Non-Destructive X-ray Characterization of Wide-Bandgap Semiconductor Materials and Device Structures

A dissertation submitted in partial fulfillment of the requirements for the degree of Doctor of Philosophy at George Mason University

By

Nadeemullah A. Mahadik
Bachelor of Science
Old Dominion University, 2003

Director: Mulpuri V. Rao, Professor
Electrical and Computer Engineering

Fall Semester 2008
George Mason University
Fairfax, VA

DEDICATION

This work is dedicated to my parents, Mr. Anwar Ali Khan Mahadik and Mrs. Noorbanu Anwar Mahadik for all the love and support, without which this work would not have been possible.

ACKNOWLEDGEMENTS

First and foremost, I would like to thank my advisors, Prof. Rao Mulpuri, and Prof. Syed B. Qadri in their guidance and support throughout my graduate studies. I am grateful for their encouragement to instill in me the drive to conduct research and solve fundamental scientific problems.

I gratefully acknowledge the support from the following grants that made this work possible: Army Research Office (Dr. Prater) under Grant # W911NF-04-1-0428, National Science Foundation under Award # ECS-0618948.

Thanks are due to Dr. Siddharth Sundaresan (GeneSiC Semiconductor), Dr. Madhu Gowda (GMU), Dr. Albert Davydov (NIST), Dr. Jaime Freitas (NRL), Dr. Abhishek Motayed (NIST), Dr. Steven Binari (NRL), Dr. Michael Miller (NRL), Hany Issa (GMU), and Geetha Aluri (GMU). Each has helped me greatly in this work.

I appreciate my dissertation committee members, Professors Dr. Mulpuri, Dr. Qadri, Dr. Sutton, Dr. Berry, and Dr. Schreifels for their time and efforts in this work.

I would like to greatly thank my wife, Mrs. Fatma Cobb, my sisters, Mrs. Ghazala Mahadik and Ms. Fazeela Mahadik, and my friends Mr. Mohammed Khaleeluddin and Mr. Ayaz Sheikh for their love and support during my entire graduate studies.

TABLE OF CONTENTS

LIST OF TABLES

LIST OF FIGURES

ABSTRACT

NON-DESTRUCTIVE X-RAY CHARACTERIZATION OF WIDE-BANDGAP SEMICONDUCTOR MATERIALS AND DEVICE STRUCTURES

Nadeemullah A. Mahadik, PhD

George Mason University, 2008

Dissertation Director: Prof. Mulpuri V. Rao

In this work non-destructive x-ray characterization techniques have been used to study undoped and intentionally doped bulk and epitaxial layers, and device structures of wide bandgap semiconductor materials, GaN and SiC. Novel non-destructive x-ray characterization methods were developed to evaluate the uniformity of strain in AlGaN/GaN device structures across the wafer and the results were correlated with device electrical characteristics. In-situ bias induced strain measurements were also carried out for the first time on the AlGaN/GaN Schottky diodes to estimate change in piezoelectric polarization charge at the heterojunction interface with the gate bias voltage.

A variety of high resolution x-ray measurements were performed on freestanding Gallium Nitride (GaN) films grown by three different laboratories using hydride phase vapor epitaxy (HVPE) technique. The lattice parameters of the quasi-bulk films were obtained using high-resolution x-ray diffraction spectra. The crystalline quality of the films was determined by measuring the x-ray rocking curves and by ^{71}Ga nuclear

magnetic resonance (NMR) technique. The anisotropic in-plane strain was determined using a novel grazing incidence x-ray diffraction technique (GID) and conventional x-ray diffraction measurements. Based on these measurements the best free standing films have surface strain anisotropy of 4.0791 x 10^{-3} up to a depth of 0.3 μm and the dislocation density is in the range of 10^5-10^7 /cm^2. High resolution x-ray topography (HRXT) measurements were also performed on the freestanding GaN films. Complete mapping of defects for the entire surface of the GaN films was obtained in a non-destructive way. From these measurements, the lateral dimensions of crystallites and cavities in the films are in the range, 200-500 nm, and 0.5-400 μm, respectively. The GaN films were found to be warped with a radius of curvature of about 0.5 m. The warpage is attributed to thermal mismatch between GaN and the sapphire substrate during growth. The characteristics of freestanding GaN films measured in this work are detrimental to the fabrication of high-speed devices such as high electron mobility transistors (HEMT) because their performance is highly dependent on the surface and interface quality.

High resolution x-ray measurements were also performed on Al^+ ion-implanted 4H-Silicon Carbide (SiC) epitaxial layers, before and after 30s ultra-fast microwave annealing in the temperature range 1750-1900 ^oC, to examine the crystalline quality of the material. Based on the FWHM values of the rocking curves, an improvement in the crystalline quality of the microwave annealed samples was observed compared to the conventional furnace annealed sample. The sample annealed at 1900 ^oC showed the best rocking curve FWHM of 9 ± 2 arcsecs, which not only confirmed annihilation of the defects introduced during the Al^+ ion-implantation process, but also an improvement in

crystalline quality over the as-grown virgin 4H-SiC sample that had a rocking curve FWHM of 18.7 ± 2 arcsecs. The theoretical and measured rocking curve FWHM values were obtained and correlated with the depth dependent microwave absorption in the SiC epilayer. These results are very significant for optimizing the annealing parameters to achieve the highest possible implant activation, carrier mobility and crystal quality.

Magnesium ion-implantation doped GaN films were also characterized using x-ray diffraction measurements after microwave annealing in the temperature range of 1300 ^{o}C – 1500 ^{o}C for 5 – 15 s. The FWHM values of the in-situ Mg-doped samples did not change with the microwave annealing for 5 s anneals. The electrical measurements on these samples also showed poor electrical activation of the Mg-implant in the GaN films. These results may be due to the presence of a high concentration of implant generated defects still remaining in the material, even after high temperature annealing for 5 s. From the FWHM values, the 15 s annealing showed an improvement in the crystalline quality of the GaN samples. Also the x-ray diffraction measurements show activation of the Mg implant. Electrical conductivity was observed in these samples, which is due to significant improvement in the crystalline quality and sufficient activation of the Mg implant.

In this work, x-ray measurements were also performed on AlGaN/GaN device structures to study the effect of localized strain on the transport measurements across the wafer. The map of in-plane strain of the AlGaN/GaN HEMT wafer showed a one-to-one correspondence with the variation in electrical resistivity. The in-plane strain variation is

in the range of $2.295x10^{-4}$ – $3.539x10^{-4}$ resulting in a sheet resistance variation of 345 - 411 Ω/□.

The in-situ high resolution x-ray diffraction measurements, performed on the AlGaN/GaN device structures under variable bias conditions, showed in-plane tensile strain for forward bias conditions, and compressive strain for reverse bias. A linear variation in the strain was observed with the bias voltage, which results in a change in the piezoelectric charge at the AlGaN/GaN interface with bias. This variation needs to be considered for the correct modeling of the device transport characteristics.

1. INTRODUCTION

1.1 Materials characteristics of gallium nitride and silicon carbide

High-power, high-frequency and opto-electronic applications like power conversion, microwave and millimeter wave reception, blue light emission, etc. have received much attention in the past decade. These applications are increasingly being used in the telecommunication, transportation, aerospace, power transmission, information storage, and various other industries. Wide bandgap materials offer numerous benefits over silicon (Si) due to their favorable material properties. Advantages of the wide bandgap materials over Si and gallium arsenide (GaAs) include:

1. Higher breakdown voltages (>1000 V) due to the larger breakdown electric field.
2. Better thermal conductivity, which results in easier cooling of the devices, and consequently reliable device operation.
3. Unipolar devices like metal oxide semiconductor field effect transistors (MOSFETs) fabricated in wide bandgap semiconductors have thinner depletion regions and have lower on-state resistance, thus reducing conduction losses and increasing the power efficiency. Thus, the disadvantages such as higher power losses in Si-based bipolar devices like insulated gate bipolar transistors (IGBTs)

and PiN diodes can be avoided by replacing them with the wide-bandgap semiconductor unipolar devices like MOSFETs and schottky diodes.

4. Wide bandgap semiconductor based devices also have lower switching losses due to better reverse recovery properties. Hence, these devices can be operated at higher frequencies.

The material properties of the two wide bandgap semiconductors of interest, namely gallium nitride (GaN) and silicon carbide (SiC), in comparison with the traditional semiconductors like Si and GaAs are given below in Table 1.

Table 1: Material properties of SiC and GaN, in comparison with those of Si and GaAs.

	Si	**GaAs**	**6H-SiC**	**4H-SiC**	**GaN**
Bandgap (eV)	1.12	1.43	3.02	3.2	3.4
Breakdown field (kV/cm)	300	400	2500	2200	2000
Electron mobility (cm^2/V.s)	1500	8500	500	1000	1200
Hole mobility (cm^2/V.s)	600	400	100	115	850
Saturation velocity (cm/s)	1×10^7	1×10^7	2×10^7	2×10^7	2.2×10^7
Thermal conductivity (W/cm.K)	1.5	0.46	4.9	4.9	1.3

The Gallium Nitride (GaN) is a wide bandgap material and has become very important because of its potential electronic, optoelectronic, high-temperature, and high-power applications [1, 2]. GaN has a hexagonal wurtzite (α-GaN) structure with a direct band gap of 3.4 eV. It also exists in a metastable cubic zinc-blende phase (β-GaN) having a slightly lower band gap (3.2 eV). Due to its direct bandgap, GaN is very useful for opto-electronic applications such as blue LEDs. Also, GaN has higher bandgap compared to SiC, and higher carrier mobilities, hence GaN offers best performance in high frequency devices. The GaN is also suitable for the growth of heterostructures using $Al_xGa_{1-x}N$ of variable Al concentration to fabricate high electron mobility transistors (HEMTs). These HEMT structures exhibit very high electron mobilities (>1500 $cm^2/V.s$) due to quantum confinement of the electrons and the tunneling phenomena in the 2 dimensional electron gas (2DEG) at the AlGaN/GaN interface. These device structures can be used for very high frequency (THz range) applications [3, 4]. Another attractive feature of GaN is the possibility of inherent spontaneous and piezoelectric polarization-induced three-dimensional doping [3, 4]. The strong piezoelectric effect and a large spontaneous polarization allow for the incorporation of a large electric field (> 10^6 V/cm) and a high sheet charge density (> 10^{13} cm-2) without any intentional doping. This indicates a potential for fabrication of high-performance and high-power microwave devices.

The SiC is another wide bandgap semiconductor material widely used for its application in high-power, high temperature and high frequency devices, and also for its chemically inert and diamond like characteristics [5]. The SiC has various polytypes of

which the 3C, 4H and the 6H polytypes are the most prominent. The 3C polytype has a cubic zinc-blende type structure and has a much lower bandgap (~2.4 eV). The 6H and the 4H-SiC polytypes have a wurtzite type hexagonal structure with higher bandgaps, 3 eV and 3.2 eV respectively. The fabrication of the 4H-SiC polytype needs precisely controlled growth conditions and has been commercially available. This polytype has the highest bandgap, and carrier mobilities among the SiC polytypes as seen from Table 1. Also, the carrier mobilities are isotropic in all crystallographic directions for the 4H-SiC whereas it is anisotropic for the 6H-SiC. Hence, the 4H polytype is more suited for the high power devices.

1.2 Defects in gallium nitride and silicon carbide materials and devices

Gallium Nitride films are usually grown on substrates such as Al_2O_3, SiC, Si, GaAs and MgO. These films are deposited on large substrates using some variation of vapor-phase or molecular beam epitaxial growth. Due to mismatch of lattice parameters and difference in coefficients of thermal expansion between GaN and its substrates, GaN films are normally in a state of stress, which has a strong bearing on their opto-electronic properties. None of the available substrates provide an excellent match for the heteroepitaxial growth of GaN [6].

In order to reduce the number of defects found in GaN films grown on foreign substrates, recently freestanding GaN films have been fabricated [7]. Thick layers of GaN films are grown by hydride vapor phase epitaxy (HVPE) on sapphire substrates and then lifted off. Since these films are pseudo-bulk, they are expected to have better crystalline

quality and fewer defects compared to the layers on mismatched substrates due to the strain relaxation. Problems such as mismatch in coefficient of thermal expansion with the substrate can also be avoided [7]. Although the freestanding GaN films are expected to have better crystalline quality compared to the layers grown on SiC or sapphire substrates, a lot of growth and surface treatment related defects may still exist in the films due to the mismatched substrate used for the Hydride Vapor Phase Epitaxy (HVPE) growth, even though the films are lifted off from the substrate. These structural defects decrease the electron mobility [8], which is detrimental for high frequency devices; and decrease the recombination lifetime, which results in poor luminescence [9, 10]. The defects in the GaN films also result in generation of further defects in the hetero-structures grown on the GaN material causing lowering of 2DEG mobility.

Silicon Carbide also faces several challenges in order to fabricate the planar high power devices. One of these challenges is the inability to use diffusion for selective area doping to form the necessary active and body regions of the device. This is because thermal diffusion of most impurities into SiC is impractical even at temperatures in excess of 1800 ^{o}C [11, 12]. Ion-implantation is the only known method to achieve successful planar selective area doping [13, 14]. The ion-implantation process introduces ions of the desired dopant species into the SiC samples at quite high energies (keV range) causing significant lattice damage and introduction of defects, and also the dopant species rest in the interstitial sites of the SiC lattice. In order to obtain the desired device operation, the dopant species have to be electrically activated by driving them into substitutional sites in the SiC lattice to either create a free electron or a hole, and also the

lattice damage has to be removed since the defects in the SiC will lower the carrier mobility due to various defect scattering mechanisms.

1.3 Characterization of defects in gallium nitride and silicon carbide

High resolution x-ray diffraction (HRXRD) is a non-destructive technique that is very useful in obtaining the precise lattice parameters, and defect information such as strain distribution and misfit dislocation density in materials. Furthermore, spatially resolved distribution of defects can be obtained with a length scale approaching a few microns. The HRXRD measurements can also be used to observe any change in crystalline symmetry in materials. It is also very useful to characterize the implanted samples. Subsidiary peaks known as Kiessig fringes occur due to the interference of the x-rays reflected from the top and bottom faces of the finite damaged layer. The absence of these fringes in annealed material indicates removal of implant lattice damage. The thickness of the implant layer can also be measured from the HRXRD measurements.

X-ray rocking curve measurement technique is also a non-destructive method to evaluate the crystalline quality of the semiconductor materials. The full width at half maximum (FWHM) of the high resolution rocking curves is a convolution of the contributions arising due to random array of dislocations, particle size, strain and wafer curvature [15]. This measurement provides a comprehensive measure of the crystalline quality.

The high resolution x-ray diffraction and the rocking curve measurements can also be modified to obtain localized lattice parameters, localized micro-strain, and the

crystalline quality from a region of the sample. Such measurements provide unique opportunity to correlate lattice quality results with independently measured electrical characteristics of the devices fabricated on the semiconductor materials. Furthermore, in-situ characterization, using x-ray diffraction and rocking curve measurements, can also be used to understand the physical phenomenon that takes place in the device structures under variable bias conditions. These results are very helpful in developing accurate models for device operation.

Double crystal high resolution x-ray topography analysis is a non-destructive technique and is a very effective tool in evaluating the crystalline quality and its uniformity across the wafer. Information on features such as average dislocation density, surface defects and morphology, average strain, average crystallite sizes, detection of stacking faults, voids or over-growths in the crystal can be obtained from these measurements.

1.4 What is done in this work?

In this work, a variety of non-destructive x-ray characterization techniques were used to study defects in Gallium nitride and Silicon Carbide. The virgin films, doped/annealed films and the films after the complete device fabrication were characterized and the results are analyzed in this work. The results are also correlated with electrical characteristics of the devices.

Freestanding GaN films, grown using HVPE technique on c-plane sapphire and separated from the substrate using laser lift-off process at three different laboratories,

were characterized for their lattice perfection. These films are considered quasi-bulk because of the absence of the substrate, which results in a higher crystalline quality compared to the films on the substrate. Defects introduced in the epilayers on the substrate due to lattice mismatch and mismatch in thermal expansion coefficient can be minimized in free standing layers separated from the substrates. Although the free standing GaN films have lesser defects, surface polishing and the lift off process may introduce some defects in these films. These defects are characterized using both conventional high resolution x-ray diffraction and grazing angle x-ray diffraction techniques for studying the dislocation density, and any strain in the material as a function of increasing depth into the films. Furthermore, high resolution x-ray topography was performed on these films to obtain a comprehensive mapping of defects over the entire surface of the film. These measurements were performed for the first time on free standing GaN films and provided important information on the nature of defects in the films.

High resolution x-ray diffraction measurements were also performed on ion implantation doped GaN films grown on sapphire substrate. These films were doped with Mg^{+} to obtain p-type material, which is necessary for both high efficiency LEDs and many high power devices. The x-ray diffraction and rocking curve measurements were performed on the virgin, as-implanted and microwave annealed (1300 -1500 ^{o}C for 5-15 s) samples to study the crystalline quality and the defect density in these films.

Virgin, Al ion implanted and microwave annealed SiC films were analyzed using high resolution x-ray diffraction and rocking curve measurements. The SiC films were

grown homoepitaxially on SiC substrates, and implanted with Al^+ ions to obtain p-type material. These films were annealed using the microwave annealing process in the temperature range of 1700 -1900 ^oC for 30s. The x-ray measurements were performed to study the crystalline quality and the defect density in these films. The depth of the implant was checked using the Kiessig fringes obtained from high resolution x-ray diffraction measurements. The annealing process was performed in order to activate the implanted Al by moving them from interstitial sites to substitutional sites in the SiC lattice and remove the defects in the SiC films caused by the implantation process. The successful annealing schedules were determined by monitoring the rocking curve widths and the sub-lattice peak intensities in the x-ray diffraction spectra.

The AlGaN/GaN device structures were characterized using conventional high resolution x-ray diffraction, x-ray micro-diffraction, in-situ diffraction with variable applied bias and high resolution rocking curve measurements. These studies were performed in order to correlate the material characteristics of the AlGaN/GaN devices with the electrical properties. These results are very helpful in improving the design, processing conditions, and modeling of the devices.

2. X-RAY CHARACTERIZATION TECHNIQUES

In this chapter different non-destructive x-ray characterization techniques used in this work are described. Details of novel x-ray arrangements used in this work are also provided.

2.1 High resolution x-ray diffraction

X-rays were discovered in 1895 by Rontgen, who at that time did not know that they were a form of electromagnetic radiation similar to light. These rays were immediately put to use by medical professionals for x-ray radiography imaging, since they could penetrate through less dense material like skin, muscle, and tissues. Using the differing absorption of the x-rays by the dense bones and the less dense body material, doctors could identify fracture or other anomalies in the body. At this time, the physical properties of these electromagnetic x-rays were not understood. In 1912, the exact nature of x-rays was found, and x-ray diffraction by crystals was discovered.

X-rays are produced when a metal target in vacuum is bombarded with an electron beam above a certain critical power. The metal target produces x-rays of characteristic wavelengths. These spectral lines fall into sets and are referred to as K, L, and M lines. Usually, the K lines are used for x-ray diffraction measurements because

they are the most intense and also do not get absorbed easily. The x-rays are usually monochromatized either by using elemental filters or by using a perfect crystal set at the Bragg reflection to obtain the particular wavelength of x-rays.

High resolution x-ray diffraction is the only technique available to obtain the precise lattice parameters, crystal orientation, and the phases of the material in a non-destructive manner. This technique is based on observing the scattered intensity of an X-ray beam hitting a sample as a function of incident and scattered angle, polarization, and wavelength or energy. When x-rays hit an atom, they either get absorbed with emission of an electron or they cause the electrons in the atom to accelerate, which results in scattered x-rays with the same frequency as the incident beam. This is known as Rayleigh scattering. These scattered x-rays interfere with each other either constructively or destructively, producing a diffraction pattern recorded by an x-ray detector. Since x-ray wavelengths ($\lambda \sim 1.5$ Å) are comparable with inter-atomic distances (d-spacing) of most atoms, they are an excellent match to find the inter-atomic spacing in materials.

The Bragg condition is met, resulting in diffraction, when the scattered x-rays undergo mutually reinforcing constructive interference at a particular Bragg angle, θ, and the d-spacing is then given by the Bragg's law as:

$$\lambda = 2d \sin\theta \tag{1}$$

The diffraction happens due to the periodicity of atoms in a crystal lattice. When the x-rays are scattered by the atoms of a crystal in phase with each other, their individual amplitudes are summed together resulting in a diffracted beam. Hence, x-ray diffraction can only be observed from materials having a crystalline symmetry. Materials lacking

this symmetry produce scattered radiation, which is not in phase and result in a weak observable intensity. The intensity of the diffracted beam from crystalline materials can be measured in a detector, which provides the Bragg angle of diffraction. The lattice parameters of various materials can be obtained from their d-spacings obtained from the Bragg angle of diffraction. The detailed derivation of the Bragg's law can be found from the original report of Bragg [16].

The x-ray diffraction system used in this work is a Rigaku ATX-E, high resolution system, shown in figure 1. A high power (18kW) Cu rotating anode generator, which produces much higher intensity compared to sealed tube generator, is used to produce the incident x-rays. In this four crystal diffractometer, two channel cut Ge (220) crystals are used to monochromatize the incident beam in order to obtain a pure Cu $K\alpha_1$ (λ = 1.5405 Å) beam. A channel cut Ge (220) crystal can also be used to analyze the diffracted beam from the sample. This arrangement removes the horizontal divergence of the x-ray beam and provides accurate lattice parameters. The diffractometer also has an open Eulerian cradle with independent χ (tilt), and ϕ (rotation) movements and an x, y, z moving stage. This enables the user to align the sample perfectly. Additionally, in this x-ray diffraction system the maximum limit of the 2θ angle is greater than 155^o, making the measurement of lattice parameters highly accurate as given by the equation,

$$\frac{\Delta d}{d} = -(\cot\theta)\Delta\theta\,. \qquad (2)$$

This equation is obtained by differentiating the Bragg law and simplifying it. Hence it can be seen from this equation that as the Bragg angular separation, $2\Delta\theta$, becomes larger, we get better resolution and more accurate lattice parameters.

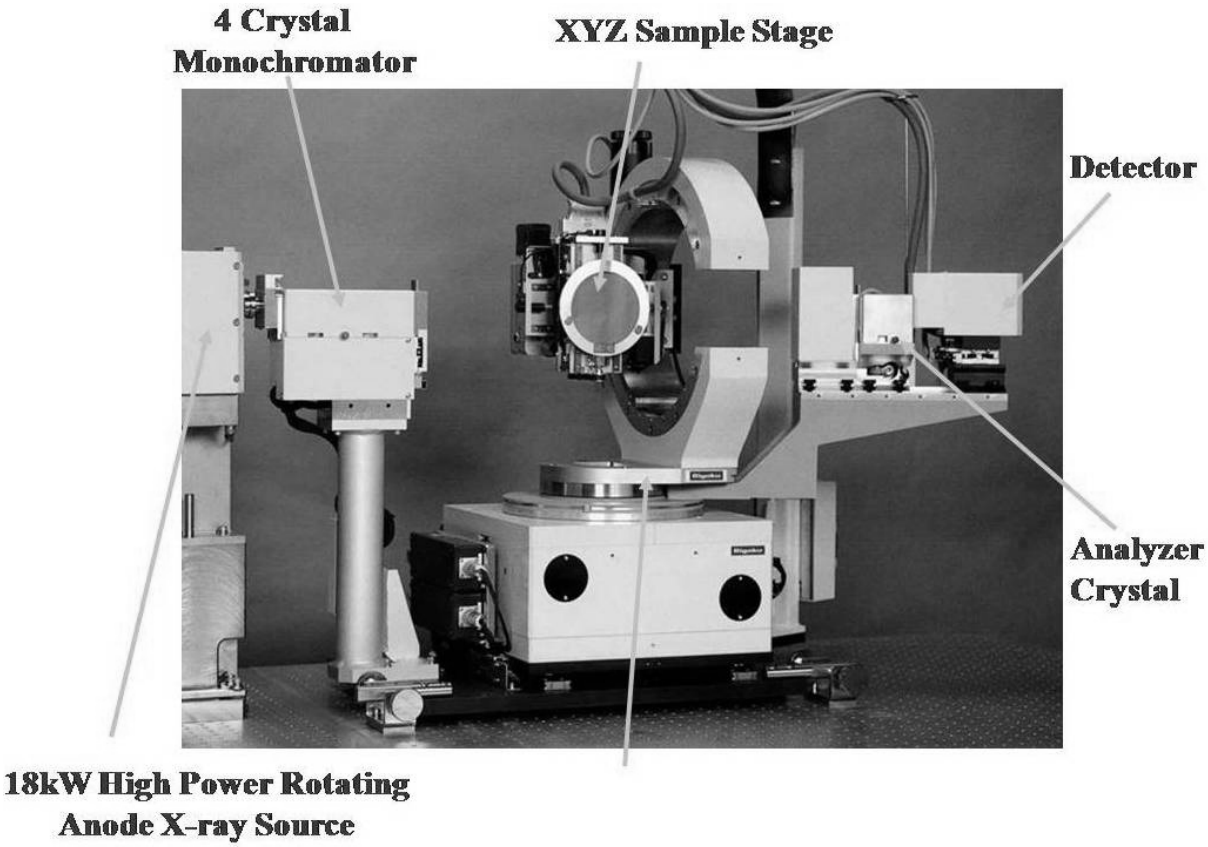

Figure 1: Rigaku ATX-E high resolution x-ray diffraction system at US Naval Research Laboratory.

2.2 High resolution x-ray rocking curve measurements

High resolution rocking curve measurements are performed on the same Rigaku diffractometer, as shown in figure 1. After the sample is mounted, perfectly aligned, and set at the Bragg diffraction angle, the single crystalline sample is rotated in the plane of the x-ray beam, over a small angle. The x-ray reflection as a function of the rotation angle is the rocking curve of the sample. The full width at half maximum (FWHM) of this spectrum is a direct measure of the average dislocation density, thickness of thin films, composition, and strain state of epitaxial single crystal films. The FWHM is broadened by the contributions arising due to random array of dislocations, particle size, strain, and wafer curvature. These individual effects can be decoupled by either taking multiple reflections or by varying the wavelength of the incident x-ray beam. Since wide bandgap semiconductors like GaN and SiC are epitaxially grown, defects such as dislocations play an important role in the performance of these materials. Hence, the rocking curve technique is very useful in characterizing the defects in these materials.

2.3 Double crystal x-ray topography

Double crystal (or high resolution) x-ray topography (HRXT) is a nondestructive technique for imaging micrometer to centimeter sized defects in crystals using a monochromatic incident x-ray beam. HRXT imaging can be done in two modes, either by diffraction, where the diffracted image of the sample is measured, or transmission mode, where the x-rays pass through the sample, and the image is obtained. In this work, diffraction topography was used. The HRXT image provides a two-dimensional spatial

intensity map of reflected x-rays. This comprehensive mapping depicts the distribution of scattering power from the crystal, revealing any defects in the lattice structure such as:

- Dislocations or bundles of dislocations.
- Crystal deformation and strain
- Voids or inclusions in the crystal
- Cracks and any surface scratches
- Phase, Twin, or Grain boundaries
- Non-crystalline areas of the wafer
- Stacking faults
- Growth striations, point defects or other defect clusters

In this technique, diffraction contrast mechanisms like structure factor, orientation contrast and extinction contrast can be used. These contrast mechanisms are presented below:

2.3.1 Structure factor contrast

The structure factor of a Bragg reflection is a mathematical description of the intensity with which a crystal scatters the incident x-ray radiation. The diffracted intensity is proportional to the square of the structure factor. The structure factor can be calculated for most reflections of a particular phase of any crystalline material. Materials with different structure factors will show different contrast in the HRXT image. Hence, materials with twin phases or domains having different structures can be characterized using this contrast mechanism.

2.3.2 Orientation contrast

If the material to be characterized has multiple crystallographic orientations, they can be identified by this contrast mechanism. The aligned regions of the sample in the Bragg condition will produce more intensity compared to the misaligned region. Multiple HRXT images recorded with different Bragg conditions will show the multiple crystallographic orientations in the sample. This contrast mechanism is useful in characterizing materials, having a small variation in the orientation of neighboring crystallites, especially observed in many epitaxial films.

2.3.3 Extinction contrast

This contrast mechanism is most useful in the characterization of defects such as dislocations, point defects, strain, etc. It was first used by Lang [17] to observe dislocations in a nearly perfect crystal, although the procedure followed was not a double crystal arrangement. Extinction contrast can be explained using the dynamical scattering theory. The diffracted beams are attenuated by both absorption and primary extinction in perfect crystal regions, but are only attenuated by absorption in the areas surrounding a defected region [18, 19]. Hence, the diffracted beam has higher intensity from the defect regions. This results in a clear contrast in the HRXT image showing the defects.

The spatial resolution of the HRXT images is governed by the relation:

$$\delta = \frac{LV}{D}, \tag{3}$$

where L is the distance of the photographic film to the sample, V is the fixed width of the incident x-ray beam, and D is the distance of the sample from the x-ray source. For the system used in this work, which is shown in figure 2, D is kept at 1.5 m in order to minimize the vertical divergence of the incident beam, and the distance L is minimized in order to get the smallest possible resolution. This system is capable of providing a resolution of ~1 μm. Also, in this system, an asymmetrically cut (111) Si monochromator is used, which is cut 1 ^{o} off the Bragg angle to provide a horizontal magnification of 26. After exposure, the films are developed and digitized to analyze the results.

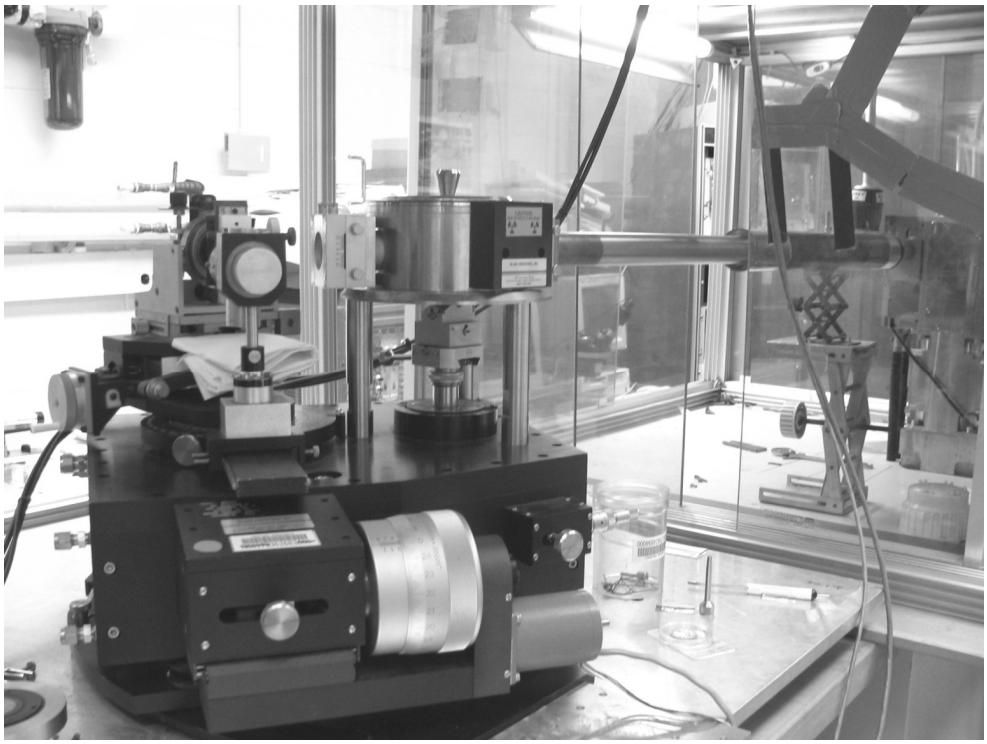

Figure 2: Double crystal x-ray topography system at the US Naval Research Laboratory.

3. Defects in Freestanding Gallium Nitride

Introduction

This Chapter deals with characterization of near surface defects in free standing GaN films grown by a recently developed HVPE method. Depth resolved x-ray measurements and x-ray topography measurements were performed on freestanding GaN films obtained from three different sources, to evaluate their quality. Grazing angle x-ray diffraction as well as conventional x-ray diffraction measurements were also performed on the films. The GaN films grown by HVPE technique on sapphire substrate were subsequently separated from the sapphire substrate using laser lift off technique.

Although there have been numerous studies on the x-ray characterization of strain in GaN films grown on sapphire substrates, not many reports exist on the evaluation of free-standing GaN films. The process of surface polishing of such films generates structural defects that may result in additional strain. These surface defects are detrimental for device performance and may eventually lead to device failure. Grazing incidence x-ray diffraction (GID) is used to measure the surface damage as a result of mechanical and chemical processing of GaN films grown by hydride vapor phase epitaxy (HVPE). In this novel technique, the x-ray beam is kept incident below the critical angle to create an evanescent wave with finite penetration depth into the sample. The depth

dependant FWHM and in-plane lattice parameters are determined. In addition, conventional HRXRD measurements are made to measure strain at greater depths. Also, a new NMR spectroscopic approach was also applied to characterize the bulk GaN films [20], relying on the sensitivity of ^{71}Ga NMR (I=3/2, 39.89% natural abundance) to effects from conduction electrons [20, 21].

In addition to the depth resolved measurements, x-ray topography was performed to obtain a complete mapping of defects in the GaN films. There have been a few reports [22-24] on investigating such defects in HVPE grown freestanding GaN, but there is no comprehensive study on complete mapping of defects for the entire surface of the films in a non-destructive way. Double crystal x-ray topography and high resolution rocking curve measurements are non-destructive techniques and are very effective tools in evaluating the crystalline quality. Information on features such as average dislocation density, surface defects and morphology, average strain, average crystallite sizes, detection of stacking faults, voids or over-growths in the crystal can be obtained from these measurements.

The surface structure of freestanding GaN films is determined using the high-resolution x-ray diffraction measurements. In addition, the possible origins of the defects such as hexagonal cavities have been explained. In this work, the warpage and the bending radius in the single crystalline freestanding GaN films is also investigated, which results from the procedure of lifting off from the sapphire substrates.

3.1 Depth Resolved Determination of Surface Strain in Free Standing GaN Films

3.1.1 Experimental procedure

Unintentionally doped freestanding n-GaN films were used for this work. They were epitaxially grown by hydride vapor phase epitaxy (HVPE) technique on (0001) basal plane sapphire substrates and subsequently the substrates were removed. The x-ray diffraction data was measured on an 18kW high-resolution Rigaku ATX-E four-circle diffractometer using CuKα_1 radiation. Rocking curves were also measured on the Rigaku ATX-E diffractometer.

Grazing incidence angle (GID) diffraction normal to the (110) basal plane, was performed to investigate the variation of the a-lattice parameter with depth as shown in figure 3.

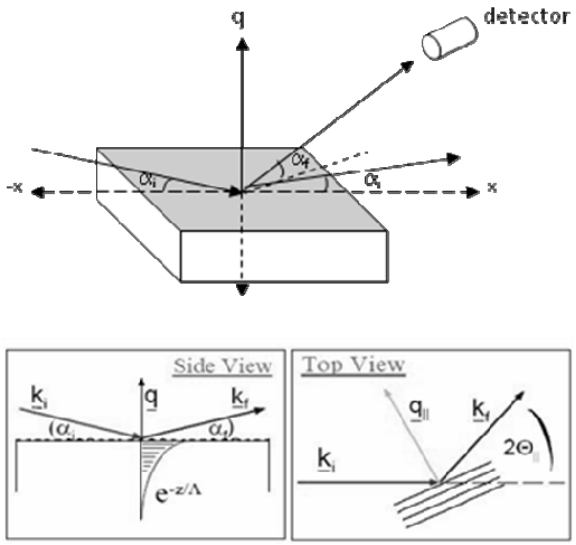

Figure 3: Experimental setup for GID measurement. k_i is the incident x-ray beam, and k_f is the diffracted x-ray beam.

The angle of incidence of the x-ray beam to the surface was varied from 0.24^{o} – 0.94^{o}. The corresponding penetration depths into the surface of the HVPE GaN were calculated using the X-Ray mass attenuation coefficient. A narrow beam of monochromatic photons with an incident intensity I_o, penetrating a layer of material with mass thickness t and density ρ, emerges out with intensity I given by the exponential attenuation law

$$I = I_o \exp\left[-\frac{\mu}{\rho}t\right] \tag{4}$$

where μ is the x-ray mass attenuation coefficient of the material for a given wavelength of the incident x-ray beam. The attenuation coefficient can be computed from equation (5) as:

$$\mu = \frac{\rho}{t}\ln\left(\frac{I_o}{I}\right) \tag{5}$$

These coefficients have been computed and tabulated for all elements in a wide range of energies. The attenuation coefficient for compounds, like GaN can be computed using the summation by atomic weight percentages of the individual elements i and is given by the relation,

$$\mu_{GaN} = \rho_{GaN}\sum_i m_i\left(\mu_i/\rho_i\right), \tag{6}$$

Now the penetration depth of the x-rays for the GID measurement is computed as:

$$depth = \frac{\sin(\theta_i)}{\mu_{GaN}} \tag{7}$$

Hence, the lattice parameters and the x-ray rocking curves of the GID peaks were obtained to get a profile of the strain distribution at varying depths.

The ^{71}Ga static nuclear magnetic resonance (NMR) spectra were obtained at a Larmor frequency of 152 MHz on a Bruker Avance DMX-500 NMR spectrometer. The samples were placed in a high-power broadband probe equipped with a 7-turn flat coil oriented so that the c-axis normal to the film, which coincides with the axis of the ^{71}Ga nuclear quadrupole coupling and chemical shift anisotropy tensors [20], could be aligned at various angles with respect to the external magnetic field of 11.7 T. The NMR measurements were performed by Dr. Yesinowski at the U.S. Naval Research Laboratory.

3.1.2 Results and Discussion

Figure 4 shows an overlay of X-Ray diffraction scans of HVPE-grown GaN for (00l) and (10l) reflections. The rocking curves were obtained for symmetric (002), (004) and (006) reflections. The c-parameter was obtained from the specular (00ℓ) reflections using the relations,

$$d = \frac{\lambda}{2\sin\theta}, \tag{8}$$

and $c = d * \ell$ (9)

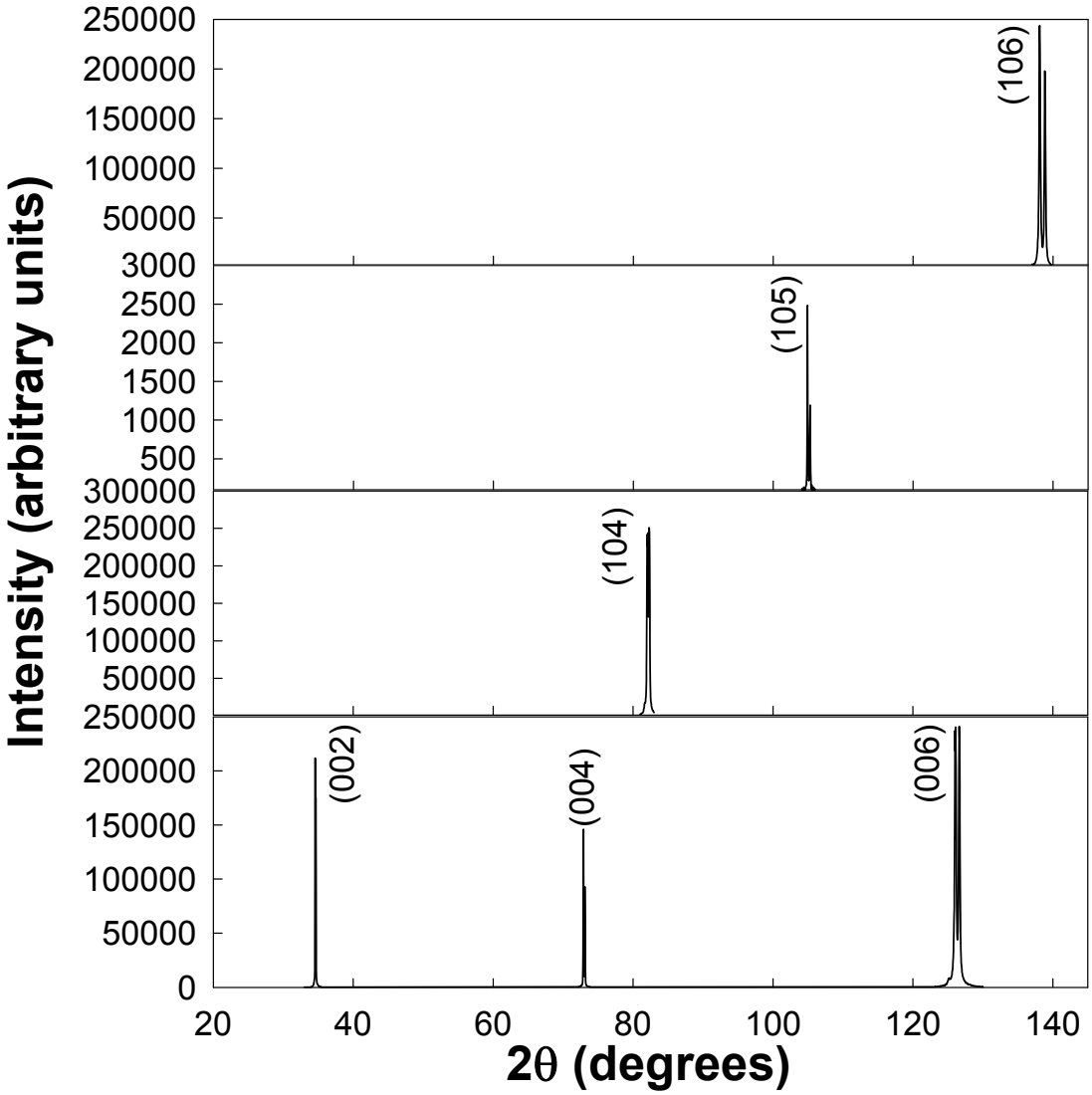

Figure 4: 2θ / θ diffraction scan of Sample A HVPE GaN

The Raleigh-Nelson correction was also applied to obtain the corrected value of c. The a-parameter was obtained from the asymmetric (10ℓ) reflections using the relation,

$$a = \sqrt{\frac{1}{0.75\left(\frac{1}{d^2} - \frac{\ell^2}{c^2}\right)}} \tag{10}$$

The results, in Table 2, show that the c- and a- lattice parameters for all three samples are similar to the GaN bulk values (c=5.1855 Å, a=3.189 Å) [25]. There is some variation in the a-lattice parameter as a function of depth from the different (10ℓ) planes, which shows depth-resolved variation in strain. The epitaxial layers exhibit good crystalline quality as determined by the narrow full width at half maximum (FWHM) of the rocking curves.

Table 2: The *c- and a*-lattice parameters for HVPE GaN 2θ-θ reflection are given. The c-parameter is the Raleigh-Nelson corrected value. ψ is the angle of incidence for the (104) and the (106) reflections. Full width at half maximum (FWHM) of the rocking curves are also specified.

Sample	**c (Å)**	**(104)**		**(106)**		**(006) FWHM**
		a (Å)	**ψ (deg)**	**a (Å)**	**ψ (deg)**	**(arc sec)**
Sample A	5.1856	3.1861	17.015	3.1874	52.071	116.98
Sample B	5.1859	3.1980	15.24	3.1883	51.047	76.978
Sample C	5.1855	3.1828	15.629	3.1819	51.361	84.78

The results from the GID measurements show an expansion in the a-lattice parameter as a function of depth and are tending towards the values obtained by conventional HRXRD measurements for higher depths of 9-25 μm. Figure 5 shows the diffraction pattern for an angle of incidence of 0.54^{o} with the surface. The variation of the a-lattice parameter with depth is shown in figure 6. It is observed that at a thickness less than 0.3 μm the enlarged a-lattice parameter remains the same, giving an in-plane strain anisotropy of 4.079×10^{-3} calculated using the relation:

$$\left| \frac{a' - a_0}{a_0} \right| \tag{11}$$

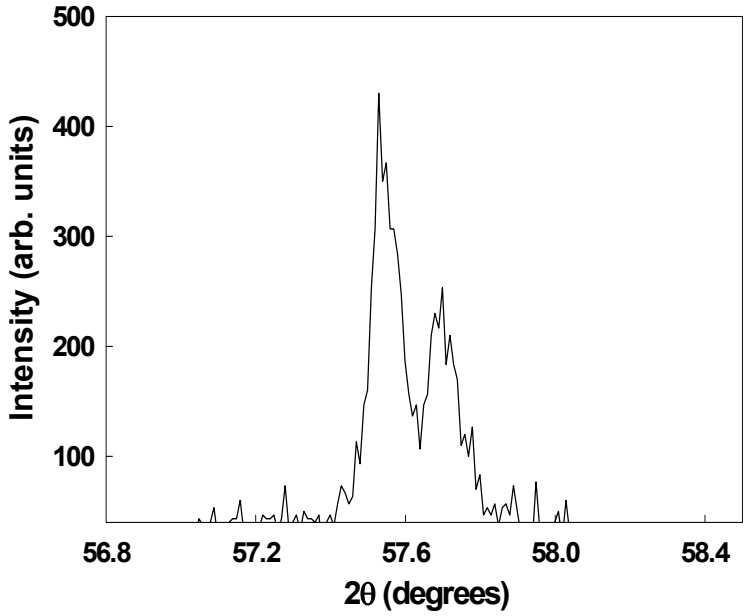

Figure 5: GID spectra of Sample A at an angle of incidence 0.54^{o} to the surface.

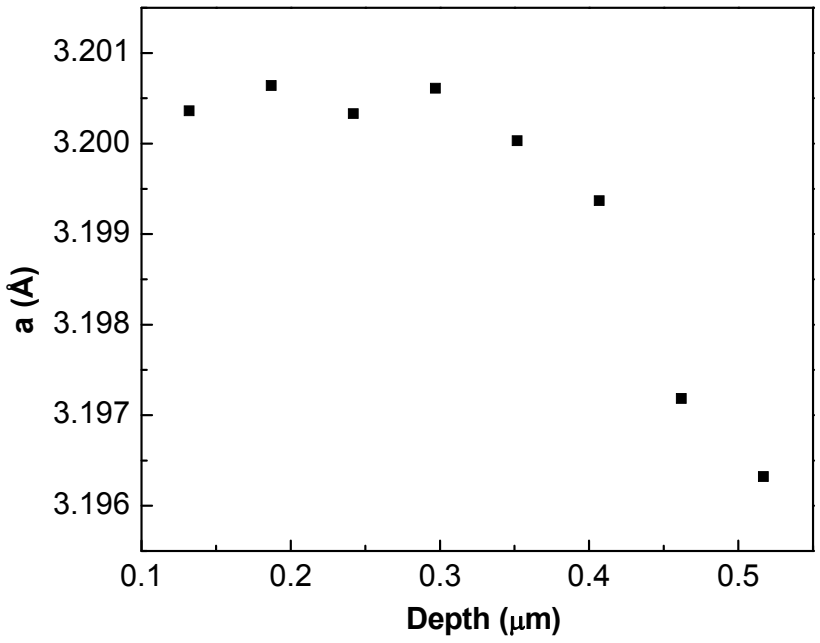

Figure 6: The variation of the a-lattice parameter with the depth from the surface.

The lattice parameter then decreases up to a thickness of 0.6 μm and relaxes to the normal lattice parameter values at the higher depths as determined by the conventional HRXRD measurements. The variation in strain as a function of depth is attributed to the surface damage as a result of mechanical and chemical polishing and processing. The FWHM of the rocking curves of the GID spectra are also shown in figure 7 as a function of depth. The decrease in the average FWHM as a function of increasing depth also suggests that the average strain relief occurs at greater depth, in agreement with the lattice parameter measurements by conventional HRXRD. Similar general behavior of lattice parameters and rocking curves was observed for the other two samples.

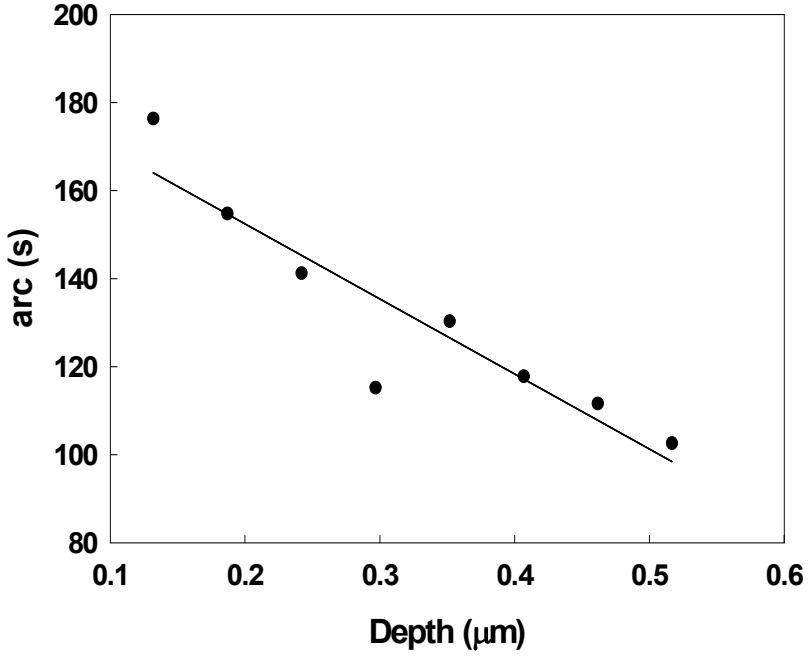

Figure 7: The variation of FWHM with depth from the surface.

The full ^{71}Ga NMR spectrum of Sample A is shown in Figure 8. A schematic energy-level diagram is included for the four-level I=3/2 ^{71}Ga spin in a high (Zeeman) magnetic field and perturbed by a nuclear electric quadrupolar interaction (arising from the presence of electric field gradients at the Ga sites) [26]. The central transition (CT) between 1/2↔-1/2 levels occurs at a spectral position known as the "chemical shift" (defined in "ppm" with respect to a reference compound); in highly-doped GaN samples, an additional shift to high frequency known as the "Knight shift" arises from the interaction of conduction electrons with the nucleus [20,21,26]. There are also two satellite transitions (ST) between ±1/2↔±3/2 levels that give rise to a doublet, whose splitting reflects the nuclear quadrupole coupling constant and hence electric field gradient, and whose linewidths increase in the presence of any distribution of these parameters due to defects.

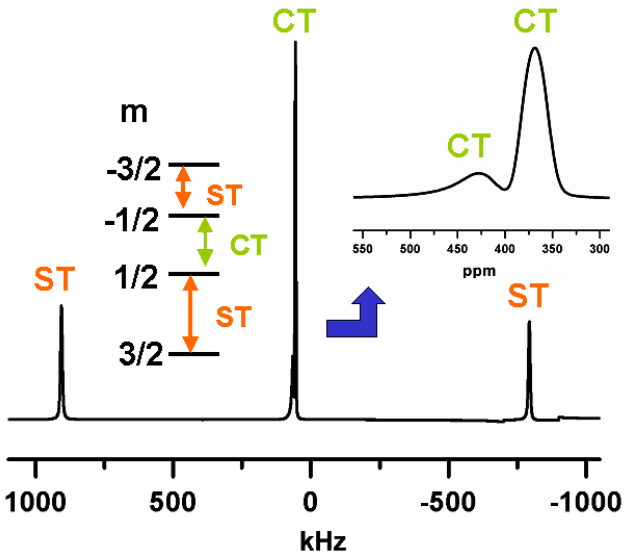

Figure 8: ^{71}Ga NMR spectrum of Sample A oriented with c-axis parallel to the magnetic field.

A CT-selective saturation-recovery pulse sequence [27] was used to measure the spin-lattice relaxation times T_1 of the left and right CT peaks shown in the inset, with resultant values of 0.34 s and 3.6 s respectively. This accords with the finding that the Knight-shifted ^{71}Ga peaks in GaN have significantly shorter T_1 values than the main unshifted peak due to Korringa-type relaxation by conduction electrons, and correspond to regions in the film with carrier concentrations above the Mott metal-insulator transition.

Fig. 9 shows ^{71}Ga spectra of the left (high-frequency) ST of Sample A, obtained with a Hahn spin echo in order to reliably observe the broad peaks, for two different values of relaxation delays, and the difference spectrum between the two spectra. The difference spectrum (7c) shows that the more rapidly-relaxing broad component extends over greater than a 100 kHz range (the true width may be broader but limited by the excitation bandwidth of the echo sequence). Observation of similar behavior for the right ST indicates that the broader ST component is associated with the rapidly-relaxing left CT peak in Fig. 8 arising from a Knight shift. Similar two-component ST peaks have been reported [20], and indicate that the regions of sample with high carrier concentrations (and hence Knight shifts) also have a *distribution* of nuclear quadrupole coupling constants and hence electric field gradients. Whether this distribution originates from substitutional dopants such as oxygen or from other types of lattice defects is not yet established.

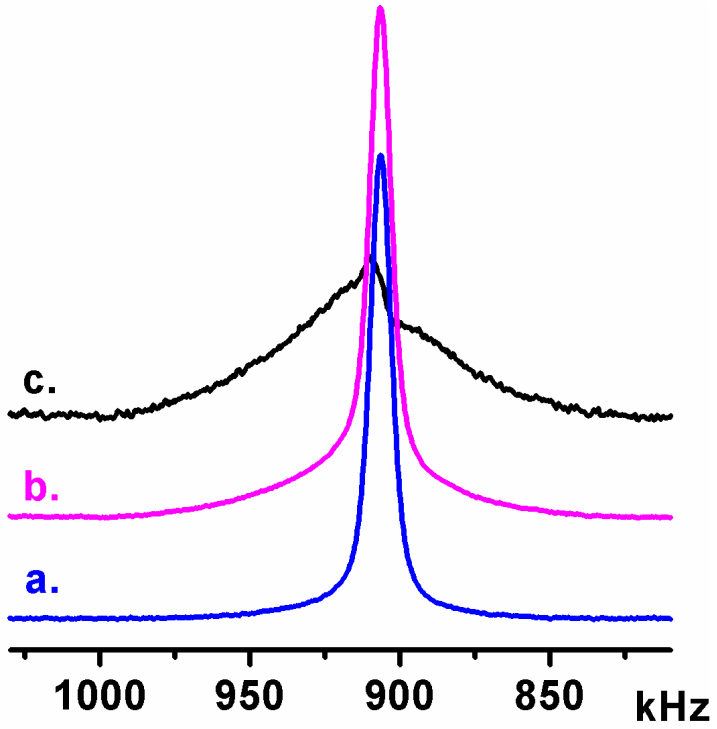

Figure 9: ^{71}Ga NMR spectra of the left (high-frequency) ST of Sample A oriented as in Fig. 8, obtained using a 90°-τ-180°-τ-Acquire Hahn spin-echo sequence

The half-height width of the fully-relaxed (long relaxation delay, i.e. quantitative) ^{71}Ga ST spectra for the three samples having a perpendicular c-axis orientation was about 7.5 kHz for Samples A and C, and 8.7 kHz for Sample B, comparable to previous values. It can be seen from Fig. 9c, a simple measurement is not very sensitive to bimodal distributions with greatly differing linewidths, as might be anticipated for sample B as well.

Figure 10 shows the fully-relaxed ^{71}Ga NMR CT spectra of all three samples for the perpendicular c-axis orientation. The differences in the chemical shift position of the

main peaks from those seen in Fig. 8 arise from a small chemical shift anisotropy and second-order quadrupolar effects. The fact that the Knight-shifted left peak of Sample A is still about 60 ppm to higher frequency from the main peak in this different orientation (Fig. 8) implies that its chemical shift anisotropy (and quadrupole coupling) must be very similar. Peak integration suggests that about 15% of the sample contributes to this Knight shifted peak, which exhibits inhomogeneous broadening due to a distribution of Knight shifts.

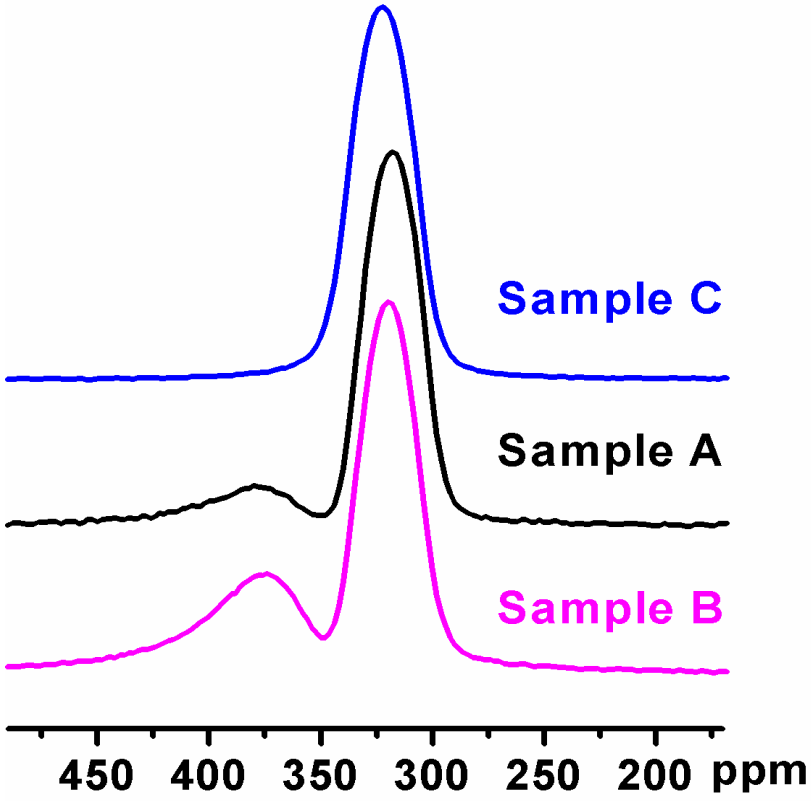

Figure 10: Fully-relaxed ^{71}Ga NMR spectra of three GaN film samples with c-axis perpendicular to the magnetic field, recycle delay = 20 s, either 90° pulses (Samples A and B) or Hahn spin-echo with delay interval = 40 μs (Sample C), line-broadening = 100 Hz. The slight 3 ppm shift to higher frequency of Sample C relative to the main peak in other samples is of uncertain significance.

Similarly large Knight Shifts have been shown in polycrystalline GaN samples to arise from degenerate electrons above the Mott transition, and the Knight shift distributions analyzed to yield probability density functions for carrier concentrations, an approach which could be applied here as well. A more intense Knight-shifted peak is observed for Sample B. The ^{71}Ga spectrum of Sample C only has, in addition to the major unperturbed GaN peak shown, a smaller shoulder to high-frequency with a shorter T_1 relaxation time (data not shown), suggesting also the existence of a much smaller Knight shift effect.

These results show that HVPE GaN film samples can contain substantial portions of the sample having much higher carrier concentrations that give rise to Knight-shifted peaks, without such regions being evident in the lattice parameters or rocking curve width measurements. Their inhomogeneous distribution makes characterization by electrical measurements difficult, but Raman micro imaging has been successfully used to observe carrier distributions in HVPE GaN films. It should also be possible to use *spatially-localized* ^{71}Ga NMR (either laterally or with vertical depth profiling) to observe the spatial distribution of Knight-shifted peaks, and thus carrier concentrations.

3.2 Study of GaN freestanding films using double crystal x-ray topography

3.2.1 Experimental Details

High-resolution rocking curves were obtained using a triple axis four-circle Rigaku ATX-E diffractometer. The HRXT measurements were taken using a double crystal arrangement, as shown in figure 11, in which the distance between the source and the first monochromating crystal was kept at 1.5 meters to minimize vertical divergence. A Si (111) crystal, asymmetrically cut 1^{o} off the Bragg reflection, was used to select CuKα radiation and to provide a horizontal magnification for the incident x-ray beam. The freestanding HVPE grown GaN samples were aligned in the (104) Bragg condition, which is close to 90^{o} with respect to the incident beam, allowing us to minimize the GaN sample to the photographic film distance giving us the highest spatial resolution. Because the GaN films were warped, only a small portion of the film diffracted at a time. To obtain the full diffraction image of the sample, a modified Schwuttke technique [28] was used. In this technique, the warped crystal is oscillated about its axis using external computer control while the image is recorded on a stationary photographic film, which is mounted parallel to the surface of crystal and at the closest possible distance to minimize vertical divergence. Thus the high-resolution topographs of the entire films were achieved by this new technique in a double crystal arrangement.

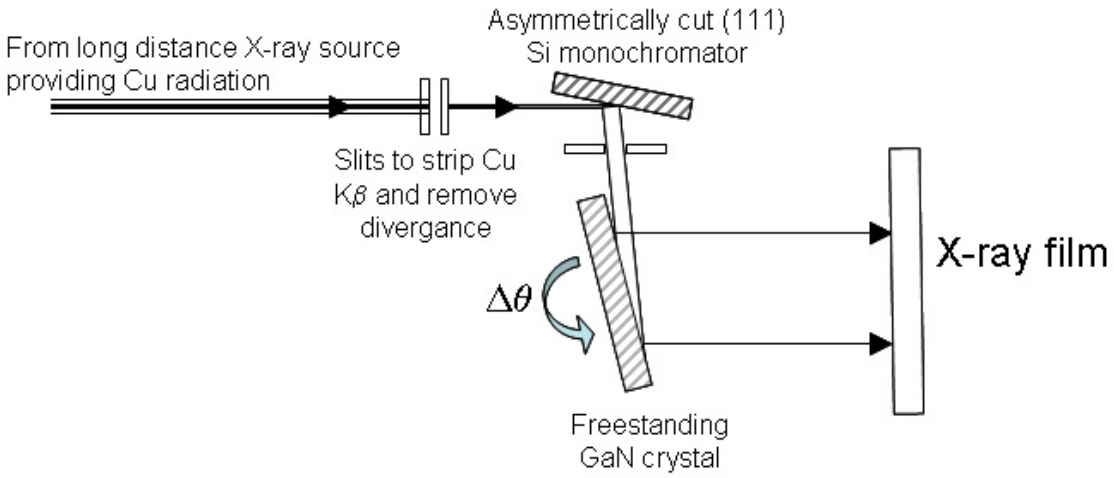

Figure 11: High resolution double crystal x-ray topography arrangement for imaging of GaN films.

In addition to HRXT measurements in which the sample crystal was oscillating, stationary HRXT images were taken to obtain the radius of curvature of the warpage in the GaN crystals. These images were also taken using the similar double crystal arrangement. The two stationary images were produced on a photographic film for a fixed angular displacement of the GaN sample. The lateral displacement between the two HRXT patterns was directly measured from the stationary images produced. This allowed us to calculate the radius of curvature for the warped film.

3.2.2 Results and Discussion

The rocking curves for the (00ℓ) reflections of the freestanding GaN samples were measured and their FWHMs (ω_i) were between 60 and 88 arcseconds for the three samples obtained from three different sources, indicating a reasonably good crystalline quality. A representative rocking curve for Sample A taken for (006) reflection is shown in Figure 12. Neglecting the contributions to the width of the rocking curves from finite particle size, the upper limit of the average dislocation density is calculated using the following equation [29-31]

$$\rho = \frac{\omega_i^{\,2}}{4.35 b^2} \tag{12}$$

where, b (~5.1855 Å) is the length of the burgers vector, which is taken as equal to c-axis lattice parameter [32]. Thus the upper limit of the dislocation density is estimated to be of the order of ~10^7 lines/cm^2 and is consistent with the topographs. The topographs tend to show a uniform intensity distribution once the dislocations exceed 10^5 lines/cm^2. Thus the dislocation density can be between 10^5 – 10^7 lines/cm^2. Similarly, assuming the contribution to the width of the rocking curve only due to finite particle size, the lower limit of the average crystallite size '*t*' of the samples can be estimated using the Scherrer equation [33]

$$t = \frac{0.94\lambda}{2\omega_i \cos\theta} \tag{13}$$

where, θ (~60^o) is the Bragg angle of the diffracting plane, and λ (=1.5405Å) is the wavelength of the incident x-ray beam. The lower limit of the average crystallite sizes for

the GaN samples in the perpendicular direction were determined to be between 340-500 nm.

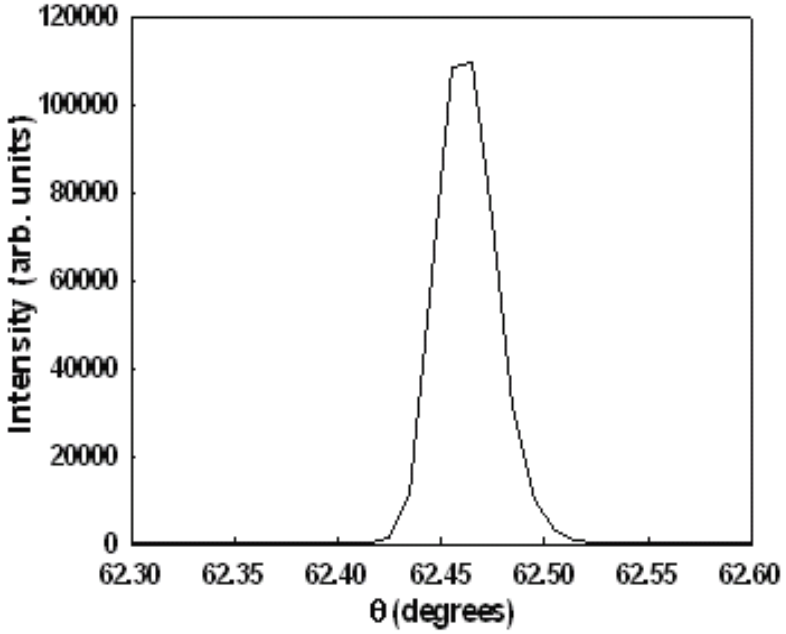

Figure 12: High resolution rocking curve for (006) GaN peak for Sample A

The HRXT images taken using (104) asymmetric reflections are shown in Figures 13 – 15 for the three GaN samples, and they reveal high dislocation densities based on the FWHMs of the rocking curves. The average lateral dimensions of the crystallites were obtained from the HRXT images, and are in the 200-500 nm range. The FWHMs of (006)

reflection and the average dimensions of the crystallites obtained from both rocking curves and topographs are given in Table 3.

Table 3: Comparison of the rocking curve FWHM's ω_i, the normal, and the lateral average grain size as measured from the rocking curves and the HRXT images.

Sample	Rocking curve FWHM	Normal crystallite size	Lateral crystallite size
A	60 arcsecs	500 nm	500 nm
B	70 arcsecs	427 nm	250 nm
C	88 arcsecs	340 nm	200 nm

In Figure 13, the HRXT image shows many surface features having dimensions in the range of 300-1000 μm. These surface features emerge due to the damage induced by post-fabrication surface polishing treatment. From the earlier GID studies we have found that the surface damage is only at the surface and extends only to a depth of 0.5 to 0.6 μm.

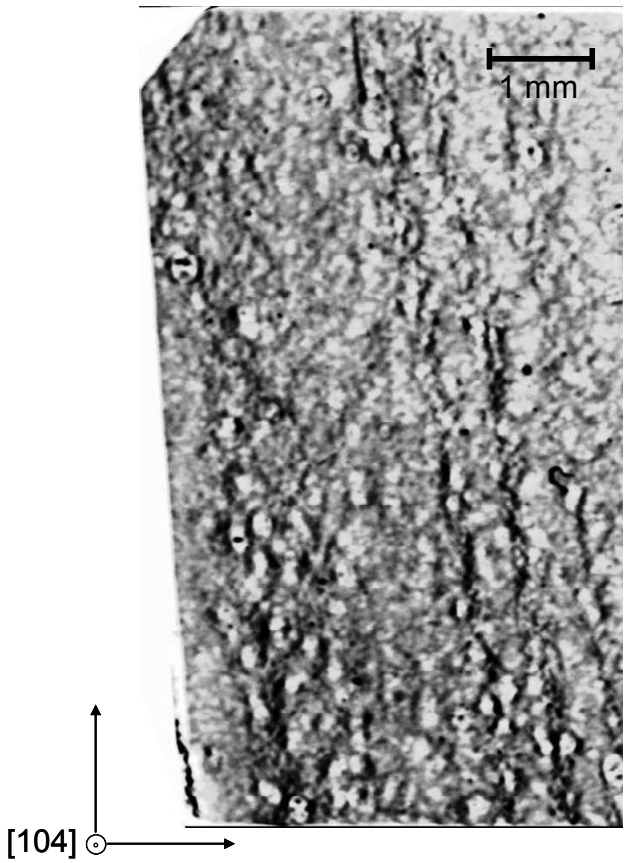

Figure 13: HRXT image for Sample A using (104) reflection. Surface features in the order of 300-1000 μm are observed.

It can be seen from figures 14 and 15 that cavities and ridges are present in the samples. The measured sizes of these cavities range from 0.5 to 400 μm. These defects are observed for the first time by HRXT, and their origin is believed to be due to the escape of nitrogen creating voids in the free standing GaN, as suggested by the TEM work of Matsubara et. al. [34].

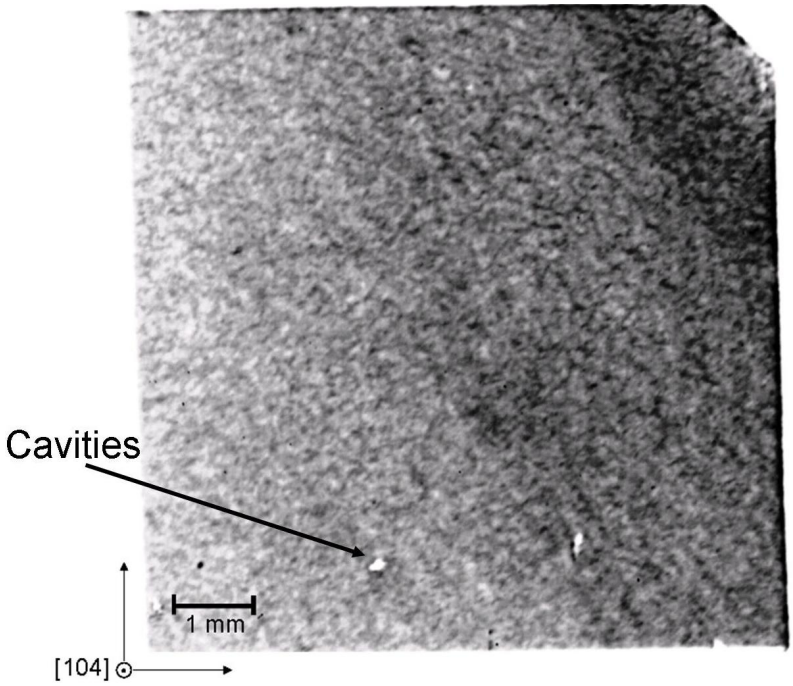

Figure 14: HRXT image for Sample B using (104) reflection. The surface is relatively smooth. Small hexagonal cavities and ridges are observed.

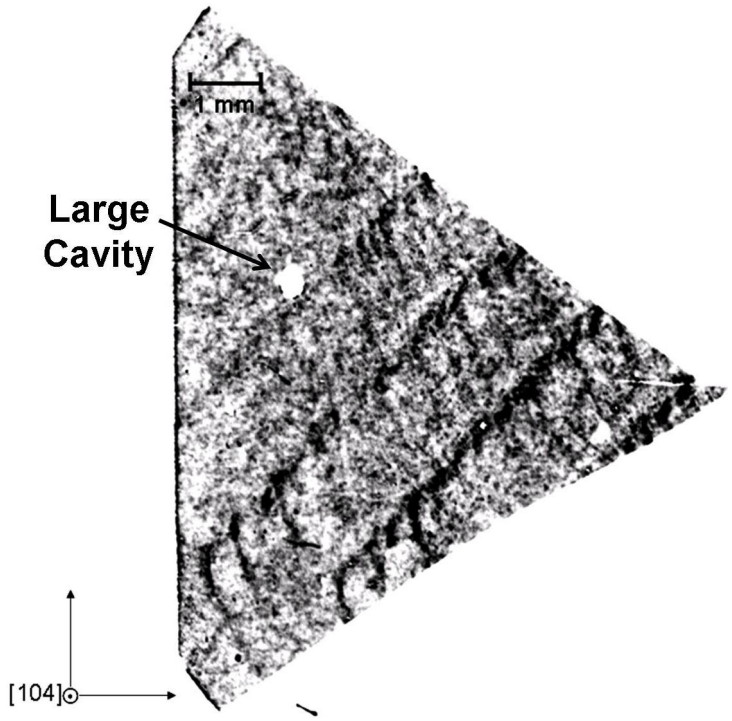

Figure 15: HRXT image for Sample C using (104) reflection. The surface is marred with ridges and large hexagonal cavities.

During the HVPE growth of GaN on sapphire, there is some nitrogen trapped by dangling bonds between the GaN epilayers and the substrate. During the laser lift-off process, it is possible that many of these dangling bonds are broken and nitrogen escapes from the films. These voids have a hexagonal core as suggested by the TEM work and such features are also observed in the HRXT images. Similar voids are also reported in an earlier study [23] by Liliental-Weber et. al. Another defect observed in these samples is the formation of ridges in the films with a periodicity of 2.375 mm and 1.66 mm, respectively, in samples B and C. It can be observed that bundle of dislocations are either

originating or terminating at these ridges. These ridge formations are also believed to be due to the effect of the laser lift-off process of the GaN films from the substrate used for the HVPE growth, which may result in the desorption and re-deposition of the GaN at the interface. This deformation may also produce numerous dislocations parallel to the interface.

Furthermore, the topographic studies showed warpage in the films. This warpage is induced due to plastic deformation causing residual strain in the HVPE grown GaN resulting from the large thermal expansion mismatch between sapphire and GaN at the growth temperature of 1073K. Once the films are lifted off, the warpage sets in due to this thermal expansion mismatch, although the GaN films are not warped originally on the substrates. The radius of curvature r of the free-standing GaN samples can be obtained from the stationary HRXT images as shown in figure 16. The displacement ℓ (~0.8 mm) in the image was measured as a function of angular displacement $\Delta\theta$ (~0.1^{o}) of the sample. Using the relation:

$$\ell = r\Delta\theta \tag{14}$$

the radius of curvature was found to be of the order of 0.5 m. From the HRXT measurements the sagittal radius s is computed, which quantifies the extent of bowing from a flat sample surface, in the GaN samples using the expression:

$$s = \frac{\ell}{2} \cdot \frac{\Delta\theta}{2} \tag{15}$$

and was found to be ~0.35μm, which is significant to produce malfunctional devices, particularly those that are fabricated in the wafer edges. The warpage induced after the

lift-off process in the GaN samples is thus detrimental to the fabrication and the yield of operational devices from a single free-standing GaN wafer. Since large area (~300mm) GaN wafers like silicon wafers are not commercially available, the effect of warpage in the GaN samples is a huge concern that needs to be seriously considered for the advancement in GaN wafer processing technology.

Figure 16: Stationary HRXT measurements showing the images after an angular displacement of the sample to compute the radius of curvature for the sample warpage.

Summary of the results

The following conclusions can be drawn from the high-resolution x-ray diffraction, grazing incidence diffraction (GID), high resolution x-ray topography and ^{71}Ga NMR studies of the HVPE-grown freestanding GaN films:

(1) The a-lattice parameter shows an expansion up to a thickness of 0.6 μm, whereas the c-axis lattice parameter is in agreement with the bulk GaN.

(2) Up to a thickness of 0.3 μm, the strain was of the order of 4.079×10^{-3}. The expansion in the lattice parameter is attributed to the defects and strain induced at the surface due to mechanical and chemical polishing.

(3) The rocking curve measurements indicate the average strain distribution is due to surface damage as a function of depth.

(4) Based on the topographs and the rocking curves the dislocation density is estimated to be in the range of $10^5 - 10^7$ lines/cm^2.

(5) Surface features were found in the order of 300-1000 μm, and cavities of the order of 0.5-400 μm were observed. The surface defects are due to the post grown surface treatments, and the hexagonal cavities can be attributed to the escape of trapped nitrogen leaving behind voids.

(6) The GaN samples are warped and have a radius of curvature in the order of 0.5m as calculated from the HRXT measurements. This curvature is due to plastic deformation and residual stress caused by a large thermal expansion mismatch between the GaN film and the sapphire substrate at the growth temperature of 1073K. This curvature causes a bowing having a sagittal radius of ~0.35μm. The

wafer curvature may be detrimental to the fabrication and yield of devices made from a single GaN freestanding wafer.

(7) A variety of ^{71}Ga NMR measurements show, in addition to the peaks expected for the highest purity c-plane GaN film sample studied by NMR[6], broad and rapidly relaxing high-frequency peaks in varying amounts for the three samples. These additional peaks arise from Knight Shifts due to conduction electrons. They reflect inhomogeneous distributions of carrier concentrations in the samples and are associated with larger distributions of electric field gradients from defects.

(8) The high-resolution conventional and grazing incidence x-ray diffraction measurements and the NMR studies provide complementary information about the quality of the film.

4. Lattice Quality of Microwave Annealed Al Ion-Implanted SiC

Introduction

In this work characterization of virgin, Al ion-implanted, and microwave annealed Silicon Carbide (SiC) material has been carried out to establish the optimum annealing parameters. Most of the devices like DMOSFETs, fabricated using the 4H-SiC polytype, require selective area doping to create p-type and n-type regions, which can only be achieved successfully by ion-implantation; but, the ion implantation process induces lattice damage and the implanted ions introduced into the SiC lattice are located mostly in the electrically inactive interstitial sites. Hence, post-implant annealing is required to remove the lattice damage and also to electrically activate the implanted species.

Typically, annealing done in conventional furnaces is relatively long (~ 5-30 mins), which may cause the SiC surface to sublimate [35] and may also introduce some new defects into the SiC sample. Ultra-rapid microwave heating technique [36] can be used to anneal the implanted SiC samples at high temperatures (>1900 ^{o}C) for a short time. Since, the microwave annealing is done for a much shorter duration (~ 30 sec), compared to the conventional furnace annealing, the SiC surface sublimation and diffusion of dopants and defects, which occur during the longer furnace annealing

process, can be avoided. The structural defects in SiC reduce the electron mobility and hence lower the current density of the power devices. In order to study the average defect density and to correlate the defect density with the annealing temperature, high resolution rocking curve measurements were used in this work to evaluate the lattice quality of microwave annealed SiC samples and to compare the results of the microwave annealing with those of conventional annealing. The full width at half maximum (FWHM) of the high resolution rocking curves is a convolution of the contributions arising due to random array of dislocations, particle size, strain and wafer curvature. It provides a comprehensive measure of the crystalline quality.

In this work, the effectiveness of the microwave annealing technique is studied, with respect to the conventional annealing, in restoring the crystalline quality of the ion-implanted SiC epilayers. It is shown how the crystalline quality at different depth locations into the sample is affected by the new microwave annealing technique. Since, the active device region in many device applications includes both the implanted and the unimplanted regions, the effect of the microwave annealing on the crystalline quality of both the regions is important for the device performance and reliability. Due to this reason, the implanted region as well as the unimplanted region underneath the implanted region was studied.

4.1 Effect of Microwave Annealing on Crystalline Quality of Al Ion-Implanted SiC Epitaxial Layers

4.1.1 Experimental procedure

Lightly doped n-type (5 x 10^{16} cm^{-3}), 6 μm thick, 4H-SiC epilayers, grown on heavily doped n-type 4H-SiC substrates, which were cut 4° off axis from the normal towards the [$11\bar{2}0$] direction, were used for this study. Multiple energy Al^{+} ion implantation was performed at 500 °C to obtain a p-type implanted layer of ~0.3 μm thickness. The multiple energy implantation schedules were designed to result in a uniform Al concentration of 1.3 x 10^{20} cm^{-3}. The implanted epilayers were spin-coated with standard photoresist, heat treated in a furnace, and microwave heated at 1050 °C in N_2 ambient for 5s to form a graphite capping layer to protect the surface of the SiC epilayers from possible sublimation during the microwave and conventional furnace annealing processes. The graphite capped samples were microwave annealed in the temperature range of 1750 – 1900 °C for 30s. For comparison conventional furnace anneals were performed at 1800 °C for 5 min. Further details on the annealing procedure are described elsewhere [37]. The graphite capping and annealings in this work were done by Dr. Siddarth Sundaresan at George Mason University.

High resolution XRD measurements were taken on an 18kW Rigaku rotating anode diffractometer using CuKα radiation. High-resolution rocking curves were obtained using the triple axis four-circle Rigaku ATX-E diffractometer. The expected FWHM values and penetration depths for the 4H-SiC samples were computed using the

dynamical scattering theory and Darwin treatment [38] for a perfect crystal. These values were correlated with the measured FWHM values obtained from the high resolution x-ray rocking curve measurements.

4.1.2 Results and Discussion

Figure 17 shows the (0,0,12) reflection XRD profiles for the graphite capped Al-implanted SiC epilayers before and after 30s isochronal microwave anneals at various temperatures. The figure also shows the XRD profile for the conventionally annealed (1800 ^{o}C/5 min) sample. All the diffraction profiles indicate very high crystalline quality as evidenced from complete resolution of the Kα_1 and the Kα_2 components of the CuKα radiation. Even in case of as-implanted sample the crystallinity remained because the implants were performed at 500 ^{o}C. The lattice parameters were calculated using the relation:

$$c = d * \ell \,, \tag{16}$$

where d is the inter-atomic d-spacing and ℓ is the Miller index and it is equal to 12 in these measurements.

For the as-implanted sample, in addition to the SiC (0,0,12) reflection, sub-lattice peaks (magnified 6 times) are observed on the low angle sides of the Bragg peak. These peaks indicate the presence of a defect sub-lattice with larger d-spacing as compared to the virgin sample caused by the implanted Al atoms occupying the interstitial lattice positions. Additionally, subsidiary peaks also known as Kiessig fringes, shown in figure 18, appear between the main peak and the defect sub-lattice. This is due to the

interference of the x-rays reflected from the top and bottom faces of the finite Al-implanted SiC damaged layer. The thickness t of the implant layer can be calculated from the equation

$$t = \frac{\lambda}{2(\sin\theta_n - \sin\theta_{n-1})} \tag{17}$$

where, λ is the wavelength of the x-rays, θ_n and θ_{n-1} are the Bragg angles of the nth and the (n-1)th Kiessig fringe. The calculated thickness of the Al-implanted layer was found to be 0.3μm, which correlates with the implantation profile from the SIMS measurements (not shown). For all the annealed samples, the disappearance of the sub-lattice peaks (Fig. 17) indicates that the implanted species are incorporated into the lattice and that the lattice damage due to implantation is removed.

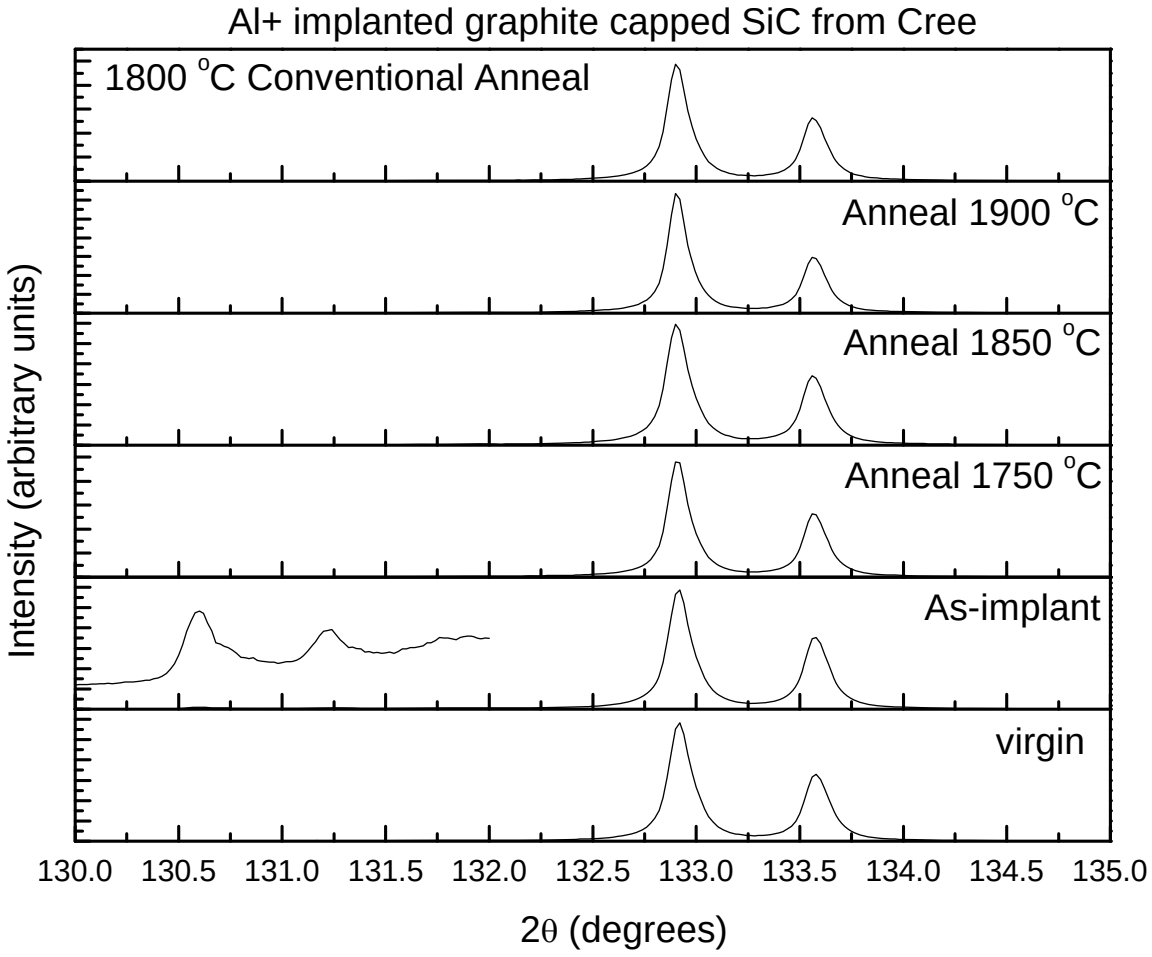

Figure 17: 2θ/θ profiles for graphite capped SiC before and after 30s isochronal microwave anneals at various temperatures.

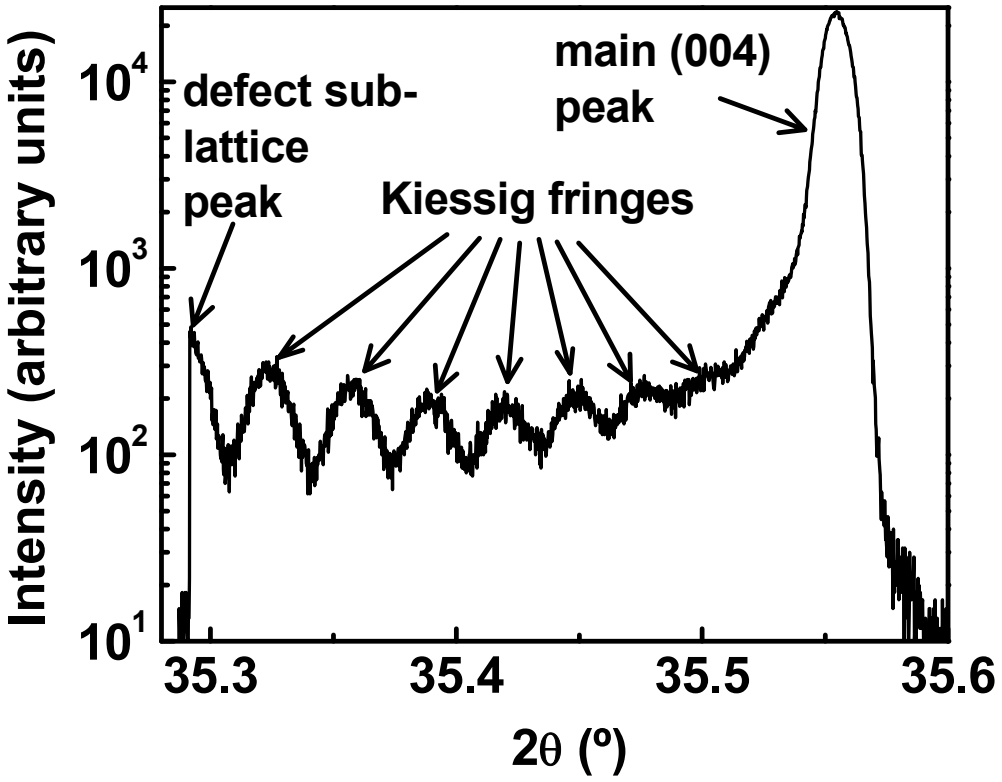

Figure 18: Narrow θ-2θ x-ray diffraction scan around the (0,0,4) reflection for the Al as-implanted 4H-SiC sample, showing subsidiary peaks known as Kiessig fringes between the defect sub-lattice peak and the main epilayer peak

Figure 19 shows the rocking curves for the (004) reflections of the virgin, as-implanted, conventionally annealed, and variable temperature microwave annealed 4H-SiC samples. The FWHMs of the rocking curves, given in Table 4, show that the as-grown 4H-SiC virgin sample has a narrow rocking curve indicating excellent crystalline quality.

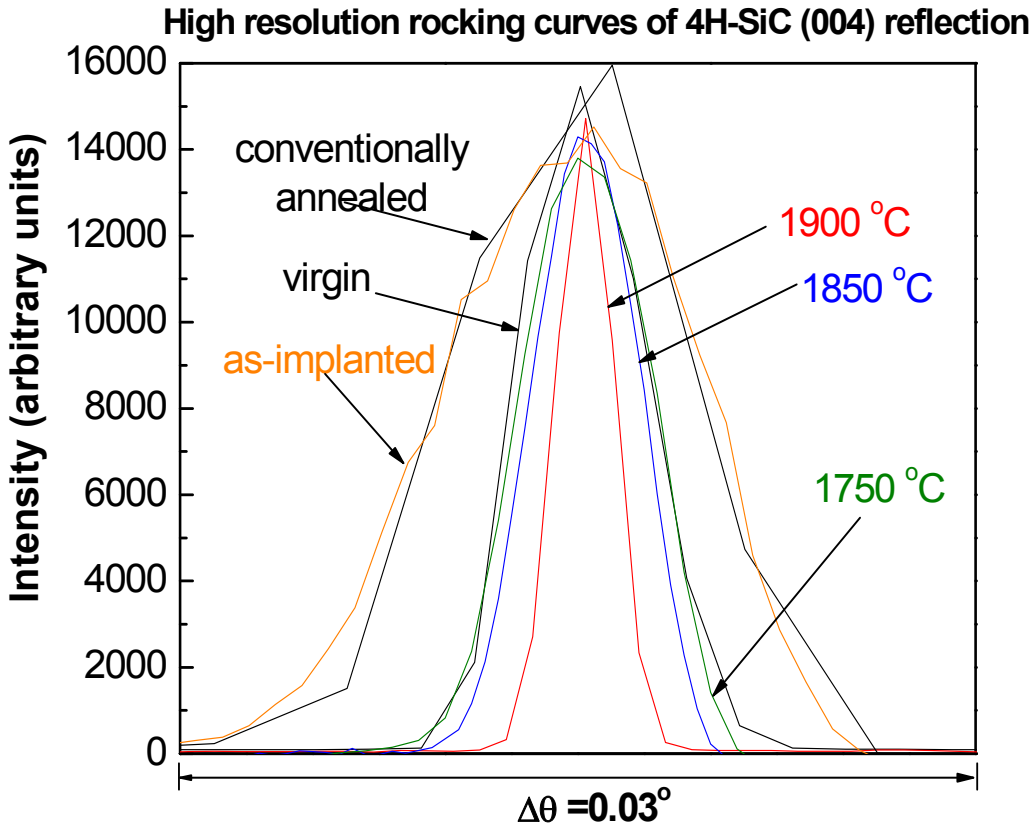

Figure 19: High resolution rocking curve using CuKα_1 (λ=1.5405 Å) radiation for (004) SiC peak for the virgin, as-implanted, conventional and microwave annealed samples.

Table 4: FWHM's of the high resolution rocking curves taken for the (004) reflection of virgin, Al as-implanted and implanted/various temperature annealed 4H-SiC.

Sample	**Virgin**	**As-implanted**	**Conv. Anneal**	**1750 °C**	**1850 °C**	**1900 °C**
FWHM (arcsecs)	18.71	41.35	34.11	20.73	16.88	9.05

After ion implantation, the FWHM increases due to the damage introduced by the implanted species in the surface region (0.3 μm) of the material. Subsequently, the microwave annealed samples showed a reduction in the FWHM for all the annealing temperatures. Although the conventional annealing process was carried out at 1800 ^{o}C for 5 mins, there seems to be a very small reduction in the FWHM as compared with the FWHM of the as-implanted sample. The electrical measurements also suggested that the microwave annealed material has better properties (lower sheet resistance) compared to the conventionally annealed material. Thus, the rocking curve FWHM values may provide a quantitative measure on the effectiveness of the microwave annealing technique in removing the implant lattice damage. Although, the conventional annealing process is successful in activating the implanted species and consequently in generating a sufficient number of carriers, a relatively high density of residual defects in the material play a very significant role in lowering the carrier mobility. This is due to defect scattering mechanisms, which affect the sheet resistance of the implanted 4H-SiC samples by ~ one order of magnitude, as reported earlier [39]. The 1900 ^{o}C microwave annealed sample shows a very low FWHM (9 ± 2 arcsecs) for the (004) SiC reflection, which is lower than the FWHM of the virgin sample (18.7 ± 2 arcsecs), indicating that the sample surface has a better crystalline quality than the virgin sample, and the microwave annealing technique is effective in removing the epitaxial growth related defects in the implanted region as well.

In order to study the crystalline quality as a function of depth, rocking curves were obtained, on the virgin sample and implanted/1900 ^{o}C microwave annealed sample,

for higher order reflections. These results were compared with the expected FWHM and the penetration depths calculated based on the dynamical theory of x-rays. The 4H-SiC has a hexagonal structure with the P63mc (186) space group and two basis atoms in the 2a and 2b positions. The positions for the atoms are given as

$$C\begin{Bmatrix} 2a & 0 & 0 & 0 \\ 2b & 1/3 & -1/3 & 0.25 \end{Bmatrix} \quad \text{and} \quad Si\begin{Bmatrix} 2a & 0 & 0 & 3/16 \\ 2b & 1/3 & 1/3 & 7/16 \end{Bmatrix}$$

The structure factor for a given reflection (hkl) is given as [40]

$$F(hkl) = \sum_r f_r \exp\left[2\pi i\left(hx_r + ky_r + l\,z_r\right)\right] \tag{18}$$

where the summation is taken for all the atomic positions. After computing the structure factors for all the required reflections for the 4H-SiC, the x-ray attenuation factor can be computed as [38]

$$\tau = \frac{\pi}{2}\left(\frac{e^2}{mc^2}\right) N\,\lambda\,|F| \tag{19}$$

where, $\frac{e^2}{2mc^2} = 2.82x10^{-13}$, N is the atoms per cm^3, λ is the wavelength of the x-rays, and |F| is the average structure factor. Assuming the intensity attenuates as 1/e, the penetration depth 't' for a given reflection is given by,

$$t = \frac{1}{\tau} \tag{20}$$

The rocking curve FWHM (in arcsecs) for a particular reflection is calculated as [38],

$$s = \frac{180}{\pi} \times \left(\frac{e^2}{mc^2}\right) \frac{N\,\lambda^2\,|F|}{\pi \sin(2\theta)} \left(\frac{1+|\cos(2\theta)|}{2}\right) \tag{21}$$

$$FWHM = 2.12 \times s \tag{22}$$

where, θ is the angle of the particular Bragg reflection. The values for the structure factors, expected FWHM, and penetration depths for the various symmetrical reflections are given in Table 5. The as-grown virgin sample has higher FWHM values than the expected FWHM for the (004) reflection, which shows the presence of growth-related defects in the epilayer.

Table 5: Calculation of the structure factor, |F|; penetration depth, 't'; and expected rocking curve FWHMs for the symmetrical reflections of 4H-SiC.

Reflection	|F|	d (Å)	θ	τ	t (μm)	Expected FWHM (arcsecs)
(0,0,4)	41.32795	2.51325	0.3115	3428.91	2.92	7.29
(0,0,8)	21.06418	1.2566	0.6598	1747.66	5.72	3.08
(0,0,12)	22.20810	0.83775	1.16671	1842.57	5.43	5.88

After microwave annealing at 1900 ^{o}C, the FWHM values are comparable to the expected FWHM values for the (004) reflection. Since, the devices to be fabricated will have their active region within the top implanted layer of ~0.3 μm, and/or in the region immediately under the implanted region, both the implanted region and the unimplanted region underneath was probed. The expected penetration depth for the (004) reflection is ~3 μm, which is an order higher than the implanted region thickness. Hence, the above

results suggest that the novel microwave annealing process has not only removed the implant generated defects, but also successfully produced a more desirable defect free SiC epilayer. For comparison, the expected and measured FWHM values of various symmetrical reflections are shown in fig. 20 for the virgin, and the 1900 ^{o}C microwave annealed samples. From the FWHM values it can be seen that the lattice quality of the top 3 μm of the implanted and annealed SiC epilayer has been significantly improved after the microwave annealing.

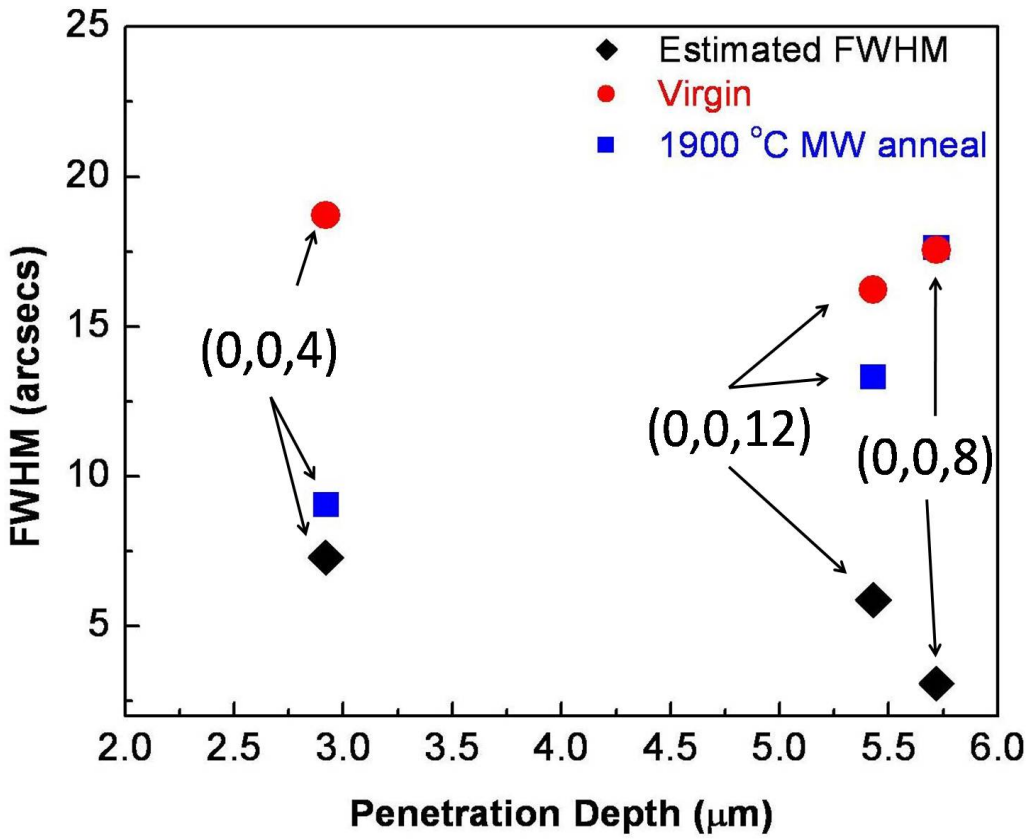

Figure 20: Measured and expected FWHM values of the virgin sample and implanted/microwave annealed sample as a function of increasing depth into the sample.

Also the FWHM of the rocking curves obtained from the reflections with greater penetration depths have either same or better FWHM values for the microwave annealed sample with respect to the virgin sample. This result can be explained by the fact that in the microwave annealing technique, the conductivity of the sample plays an important role in the absorption of the microwaves and consequently on the effective heating of the sample [36]. Since, the sample is ion-implanted only at the surface, there is a conductivity gradient across the epilayer thickness resulting in a more effective heating of the surface region of the epilayer. This result shows that the microwave annealing technique can be used successfully to obtain an implanted material having a very good crystalline quality, and also to reduce defect concentration in the epitaxial layer in which the implants are performed.

Summary of the results

High resolution x-ray rocking curve measurements (FWHM values of the rocking curves) have been used to determine the crystalline quality of the virgin and ion implanted 4H-SiC epilayers, before and after ultra-fast microwave annealing in the temperature range of 1700 – 1900 ^{o}C. The microwave annealing technique is successful in removing the lattice damage induced by the ion implantation process, and in activating the implanted species in the 4H-SiC. The microwave annealing process also appears to improve the crystalline quality of the epilayer region as compared to the virgin sample. Since, the devices are fabricated using the implanted layer or the region just below it, the microwave annealing appears to be a very promising technique for both activating the

implant and for significantly improving the crystalline quality of the entire epilayer, which will result in an excellent device performance and reliability.

5. Microwave Annealed Mg-Implanted GaN

Introduction

In this Chapter, the feasibility of microwave annealing process for achieving Mg-implant activation in GaN films is studied using HRXRD and rocking curve measurements. Using these results, the annealing parameters were optimized to obtain the best crystalline quality and highest Mg implant activation in the GaN films for the first time. Ion implantation is the only known selective doping method for GaN, since high temperature thermal diffusion leads to incongruent evaporation of GaN, which leads to creation of nitrogen vacancies. Ion-implantation also allows precise control of dopant concentration and depth distribution. Since, as grown GaN is inherently n-type a much higher implant activation of acceptor ions like Mg is necessary for realization of p-type GaN material. Unfortunately, the high implant dose introduces lattice damage, and the activated *p*-type carriers are easily trapped and compensated by the radiation defects, resulting in less effective net acceptor activation [41]. Hence, high temperature (>1200 ºC) annealing is required for removing the implantation generated defects in GaN and also to activate the Mg-implant. The GaN epilayers cannot withstand temperatures in excess of 1100 ºC for more than a few seconds, due to low incongruent sublimation temperature of N. Hence, to preserve surface morphology, the ramping rate to reach the

annealing temperature should be very fast, and the duration of the anneal should be limited to few seconds [42, 43]. A novel ultra fast microwave annealing technique, having a ramp rate of ~500 ^{o}C/s, was used to anneal the GaN samples in the temperature range of 1300 – 1500 °C for 5 – 15 s durations. Additionally, the surface of the GaN films was protected with an AlN capping layer deposited using pulsed laser deposition technique.

5.1 Effect of Microwave Annealing on Crystalline Quality of Mg Ion-Implanted GaN Epitaxial Layers

5.1.1 Experimental procedure

HVPE grown, 3 μm thick, GaN epilayers on sapphire substrates were obtained from commercial sources. Single energy (150 keV) Mg-ion implantation was performed at 500 ^{o}C to obtain a p-type implanted layer of ~0.2 μm thickness. The implantation schedules were designed to result in a uniform Mg concentration of 5 x 10^{14} cm^{-3}. A 0.6 μm thick AlN capping layer was deposited on the GaN films to protect the surface of the epilayers from possible sublimation during the microwave annealing processes. The AlN capped samples were microwave annealed in the temperature range of 1300 – 1500 ^{o}C, for 5 – 15 s durations. The AlN capping layer was removed using chemical etching before characterization.

For comparison, x-ray diffraction was also performed for microwave annealed multiple energy Mg ion-implanted GaN films. The Mg ion-implantation was performed at 500 ^{o}C, and the schedule is given in Table 6.

Table 6: Multiple energy Mg implantation schedule for GaN films

Implant Energy (keV)	**Dosage ($x10^{14}$ cm^{-2})**
10	38
25	3.3
55	1.7
110	4.1
225	8.3
300	8.3

High-resolution x-ray diffraction and rocking curve measurements were performed using the triple axis four-circle Rigaku ATX-E diffractometer. Symmetric and asymmetric reflections were obtained to calculate both the *a* and *c* lattice parameters before and after the microwave annealing process. The measured rocking curve FWHM values were used to measure the crystalline quality of the samples.

Photoluminescence (PL) studies were performed using a He-Cd laser with an excitation intensity of 2.5 mW to correlate with the HRXRD measurements. These measurements were performed by Dr. Madhu Gowda at the US Naval Research Laboratory.

5.1.2 Results and Discussion

Fig. 21 shows HRXRD spectra for the GaN (004) reflections on the as-implanted and microwave annealed multiple energy Mg ion-implanted samples. It can be seen from the HRXRD spectra that the sub-lattice defect peak for the annealed samples does not disappear. This is due to the excessive damage produced by the multiple energy implantation process in the GaN films, which cannot be reduced by the microwave annealing process.

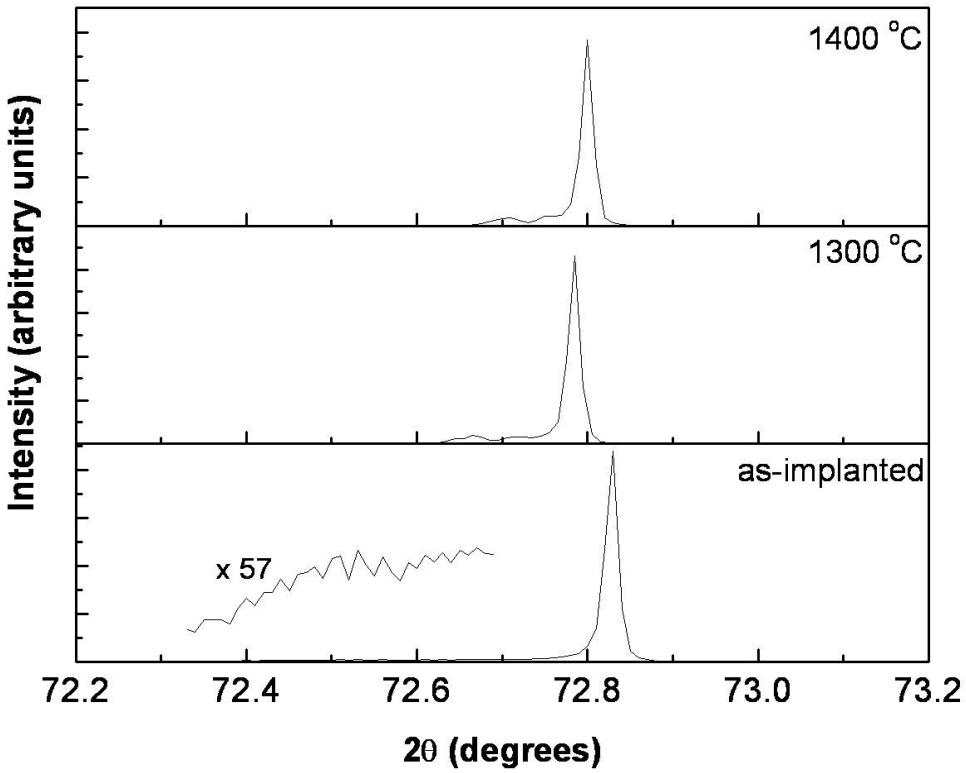

Figure 21: XRD spectra of the multiple energy Mg ion-implanted and the microwave annealed samples for 5 s duration

The lattice parameters and rocking curve FWHM values for the multiple energy Mg implanted GaN films are given in Table 7. From the FWHM values no significant improvement is seen upon annealing of these samples. Due to the fact that the multiple energy implantation process causes severe damage in the samples, single energy Mg ion-implantation was performed for further study of Mg acceptor activation in GaN.

Table 7: *c* lattice parameters and rocking curve FWHM values of the multiple energy Mg-implanted 5 s microwave annealed GaN films.

Samples	**Reflection**	**FWHM (arcsecs)**	**2θ (degrees)**	**c (Å)**
as-imp	(004)	311.8	72.829	5.1903
1300 ^{o}C	(004)	309.5	72.785	5.1931
1400 ^{o}C	(004)	297.6	72.800	5.1921

Figures 22 and 23 show HRXRD spectra for the (004) reflections on the virgin, as-implanted, and microwave annealed (15 s and 5 s, respectively) single energy Mg ion-implanted samples. The sub-lattice peak, which appeared in the as-implanted sample due to the interstitial Mg atoms in the GaN lattice, disappeared after annealing. This shows that the microwave annealing technique is successful in driving interstitial Mg atoms into

the substitutional positions. The lattice parameters were obtained from the HRXRD measurements of the symmetric GaN (004) and asymmetric (104) reflections.

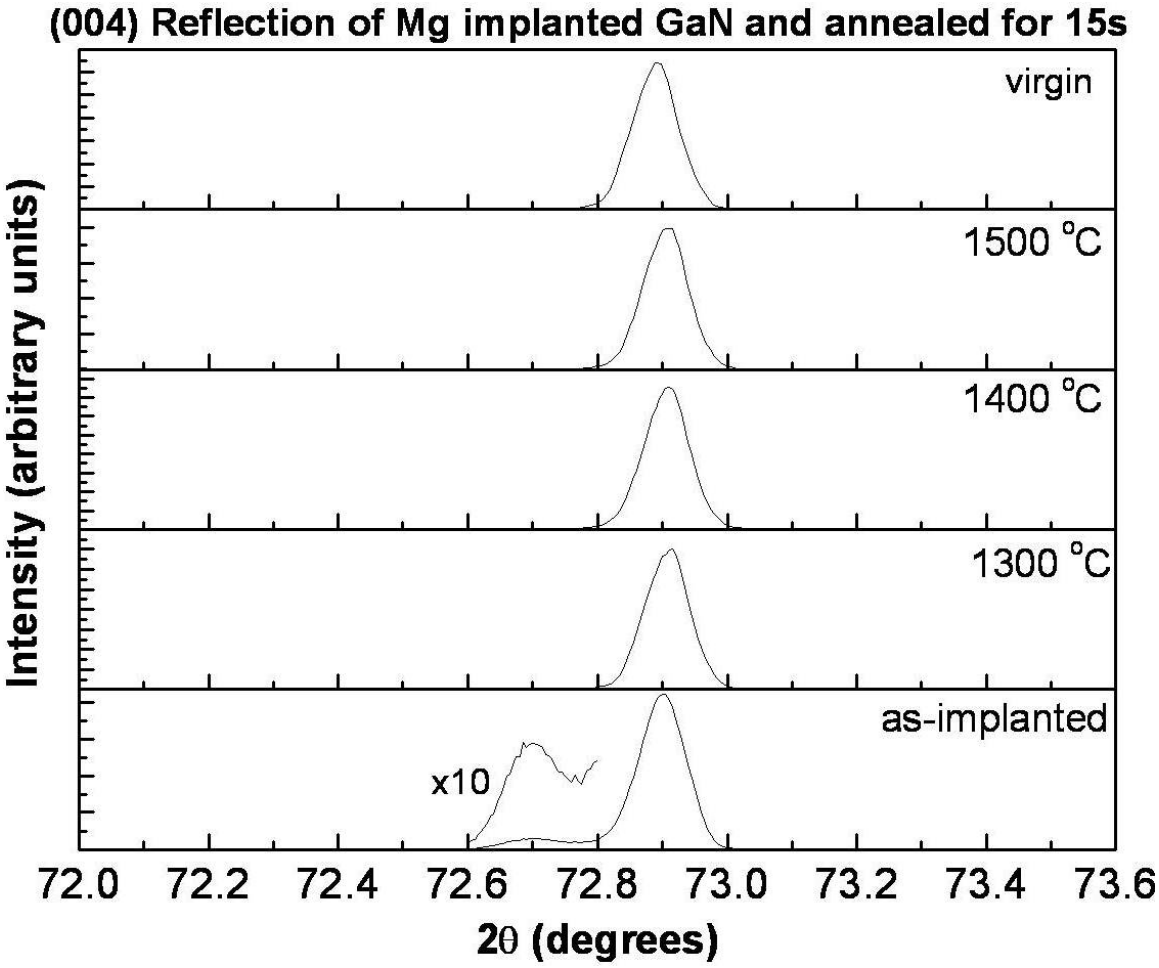

Figure 22: XRD spectra of the 150 keV Mg ion-implanted and the microwave annealed samples for 15 s duration

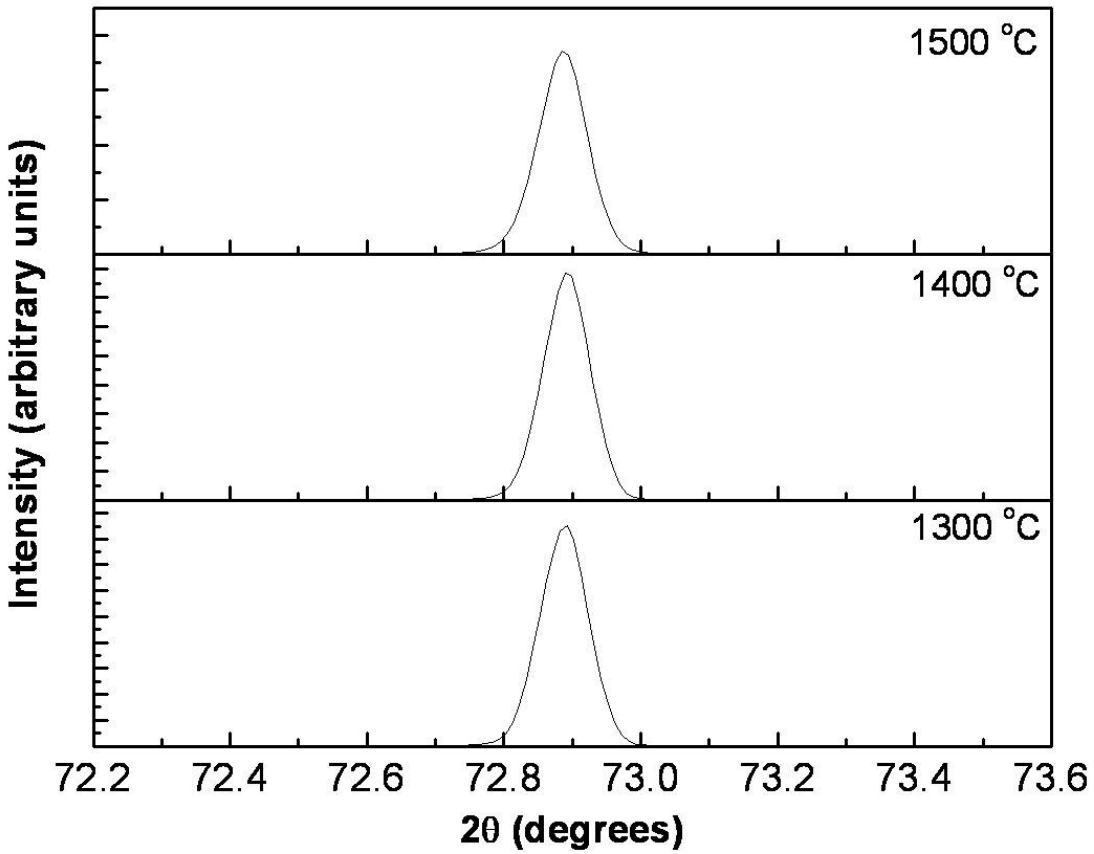

Figure 23: GaN (004) XRD spectra of the microwave annealed 150 keV Mg ion-implanted samples for 5 s duration

The *a*, and *c* – parameters were computed using the equations,

$$c = d_{004} \times 4\,, \tag{23}$$

and

$$a = \sqrt{\frac{4}{3}\left[\frac{1}{\frac{1}{d_{104}^2} - \frac{16}{c^2}}\right]} \tag{24}$$

The lattice parameters and rocking curve full width at half maximum (FWHM) values for the virgin, as-implanted, and 15 s microwave annealed samples are given in Table 8. Table 9 shows the *c* lattice parameters and FWHM values of the 5 s microwave annealed samples.

Table 8: *a* and *c* lattice parameters and rocking curve FWHM values of the virgin, implanted and 15 s microwave annealed GaN films.

Sample	**Reflection**	**θ**	**FWHM (arcsecs)**	**2θ**	**c/a (Å)**
Virgin	(004)	36.745	293.0	72.900	5.1860
	(104)	16.918	209.1	82.040	3.1890
as implanted	(004)	36.819	310.7	72.900	5.1860
	(104)	16.741	231.5	82.027	3.1915
1300 ^{o}C	(004)	36.132	273.9	72.908	5.1855
	(104)	15.545	197.6	82.036	3.1914
1400 ^{o}C	(004)	36.098	248.5	72.907	5.1856
	(104)	15.508	206.8	82.035	3.1913
1500 ^{o}C	(004)	36.732	252.8	72.906	5.1857
	(104)	16.879	207.9	82.038	3.1906

Table 9: *c* lattice parameters and rocking curve FWHM values of the 5 s microwave annealed GaN films.

Sample	Reflection	FWHM (arcsecs)	2θ	c (Å)
1500 ^{o}C	(004)	245.3	72.886	5.1869
1400 ^{o}C	(004)	225.9	72.892	5.1865
1300 ^{o}C	(004)	233.4	72.888	5.1867

The lattice parameters of the 15 s microwave annealed samples appear better compared to the 5 s annealed samples. After annealing at 15 s, both the *a*, and *c* lattice parameters of the GaN films are same as the values reported for bulk GaN material. This shows that the microwave annealing at 15 s is very successful in removing strain in the GaN films. The rocking curve measurements on the 5 s and 15 s annealed samples were performed at different times and the system was reinitialized before the measurements in each case. Hence, there is a possibility of small variation in the divergence present in the incident x-ray beam. This may cause the FWHM values to increase slightly. Hence, the FWHM values of the 15 s and the 5 s annealed samples may vary slightly and can't be compared.

For 5s annealing the lattice parameters show an expanded lattice and did not match with the bulk GaN values even after 1500 C annealing. The FWHM values also did not show a definitive improvement with increasing annealing temperature. This indicates that even though the sub-lattice peak in the as-implanted sample disappeared a significant concentration of defects still remains in the sample and are not annihilated by the 5 s annealing. Two-probe electrical measurements on these samples did not show any

evidence of Mg electrical activation as in case of multiple energy Mg ion-implanted samples. Based on the above results the annealing duration was extended from 5 s to 15 s.

Figure 24 shows the variation of the FWHM values of the implanted and 15 s microwave annealed samples. It can be seen that the FWHM values decrease with increasing annealing temperature till 1400 ^{o}C, and are same for both the 1400 ^{o}C and 1500 ^{o}C annealed samples. This shows an improvement in lattice quality and lower dislocation density for the samples annealed at temperatures $\geq$ 1400 ^{o}C for 15 s. Furthermore, from the FWHM values, the 1400 ^{o}C and 1500 ^{o}C 15 s annealed samples also show a marginal improvement over the virgin sample, as observed before for ion-implanted SiC in the previous chapter . This shows that the microwave annealing process is also successful in removal of the growth related defects.

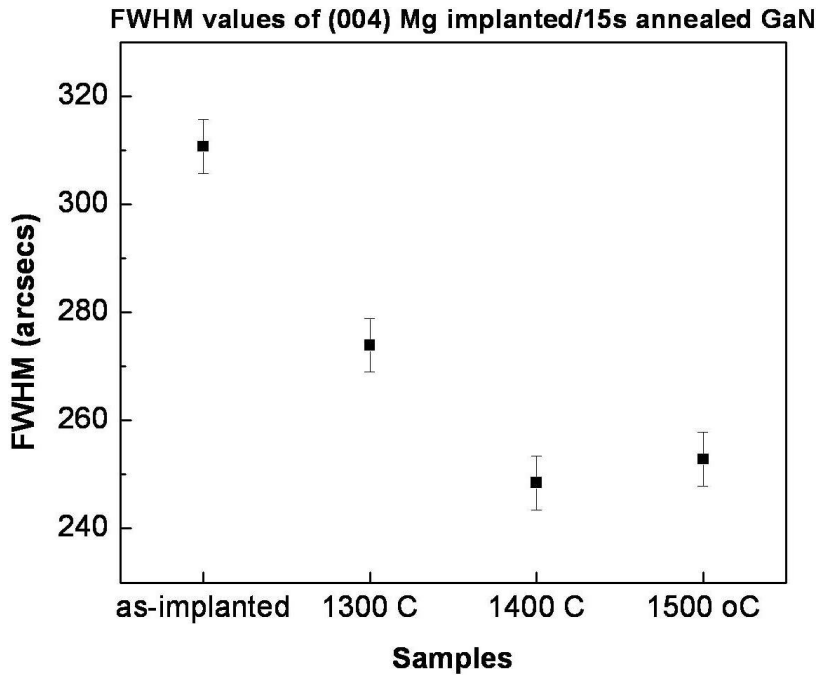

Figure 24: Comparision of the x-ray rocking curve FWHM for implanted and 15 s annealed GaN samples.

These results correlate well with two-probe conductivity measurements, shown in fig. 25 on these films, which show that the 1400 C/ 15 s and 1500 ^{o}C/15 s microwave annealed samples are conductive, whereas the samples annealed at lower temperature and time are non-conductive. Hence, we observe that the 15 s microwave annealing of the Mg-implanted samples at 1500 ^{o}C is successful in activating the Mg implant as well as improve the crystalline quality of the GaN films. The net Mg acceptor activation stems from the fact that the density of compensating donor defects in the lattice are effectively decreased by the 15 s anneals for temperatures $\geq$ 1400 ^{o}C.

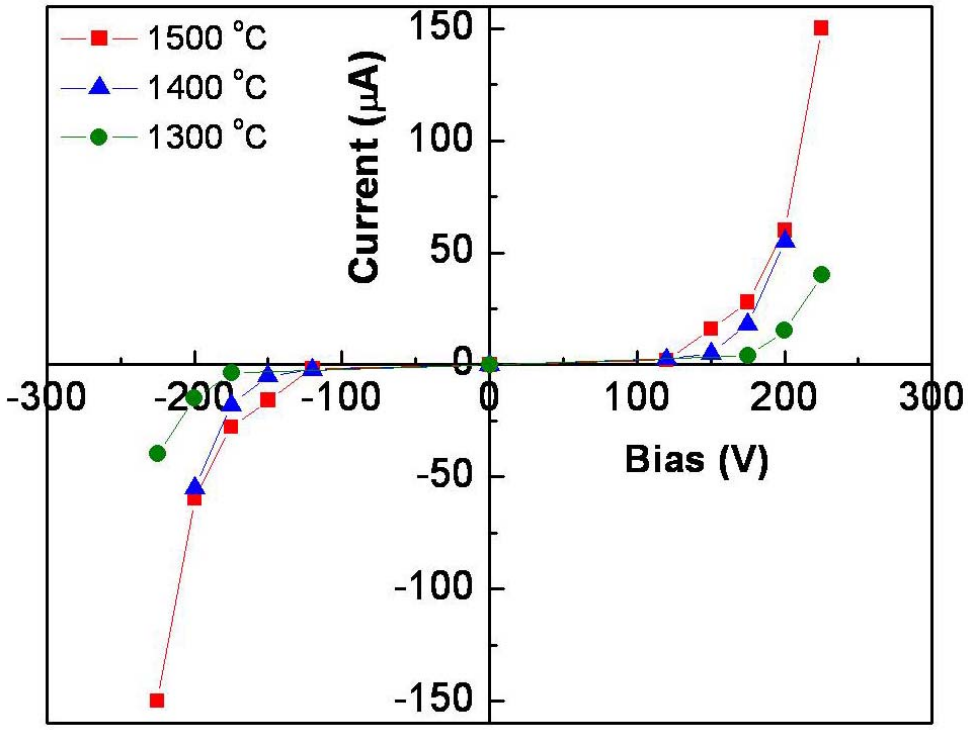

Figure 25: Two-probe conductivity measurements on the single energy Mg-implanted, 15 s microwave annealed samples.

Low-temperature PL, shown in Fig. 26, was performed on the virgin, implanted as well as 15 s microwave annealed GaN films. The PL spectra shows an increase in Mg activation for the 1300 ºC / 15 s annealed film by the presence of an intense Ultra violet light (UVL) band at 3.29 eV zero phonon line (ZPL) as well as a relatively stronger near-band-edge emission (NBE) band at 3.46 eV with its phonon replica (1LO-NBE) at 3.37 eV. Upon increasing the annealing temperature to 1400 ºC/15s and 1500 ºC/15s, the intensity of NBE band decreases with an increase in the intensity of broad near-UVL band (2.7 – 3.1 eV). A broad yellow luminescence is also observed (2.0 –2.4 eV) in the

spectra of the annealed sample. An increase in the intensity and structure of the Donor-Acceptor Pair (DAP) band with increasing temperature is also observed. These results also correlate well with that of the HRXRD and two-probe electrical measurements, and confirm the increase in the concentration of Mg acceptors at higher annealing temperatures.

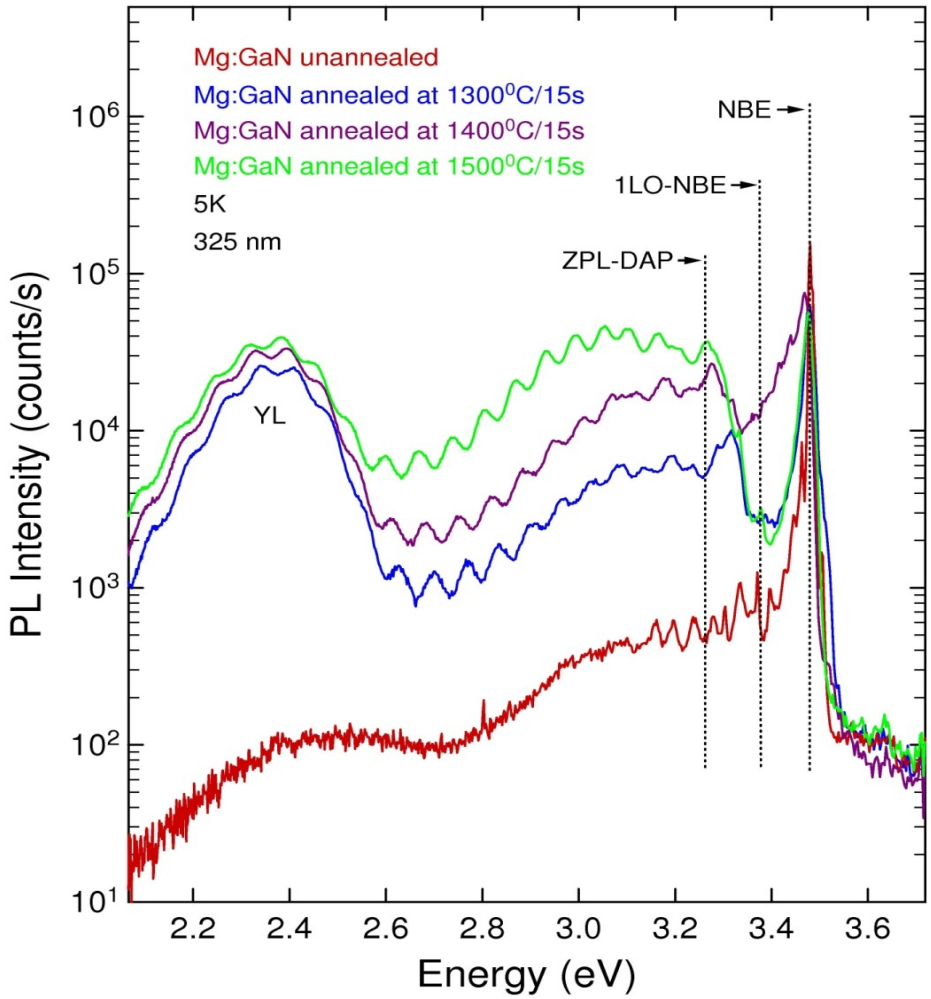

Figure 26: Low-temperature (5 K) PL spectra of virgin, as-implanted and microwave annealed Mg-implanted GaN grown on sapphire; for 1300 ºC, 1400 ºC, and 1500 ºC. All anneals were performed for 15 s.

Summary of the results

High resolution XRD and x-ray rocking curve measurements were used to optimize the annealing parameters for achieving the best crystalline quality and highest implant activation in Mg implanted GaN films. The crystalline quality was determined for the virgin, as-implanted, and ultra-fast microwave annealed GaN epilayers in the temperature range of 1300 – 1500 ^{o}C for 5 – 15 s durations. Based on the disappearance of the sub-lattice peak in the HRXRD spectra and an improvement in the FWHM values, the microwave annealing technique is found to be successful in removing the lattice damage induced by the Mg ion implantation process, and in activating the implanted Mg in the GaN films. This behavior, however, was observed only for single energy implanted samples for an annealing temperature $\geq$ 1400 ^{o}C for a duration of 15 s. In case of multiple energy Mg-implantation even 15 s annealing couldn't result in any Mg activation due to large degree of lattice damage, which introduces compensating donor levels. The microwave annealing done at 1500 ^{o}C for 15 s also appears to improve the crystalline quality of the epilayer below the implanted region as well. The crystalline quality and percent of implant activation is very important in operation of the high power and high frequency devices in the GaN films. Hence, optimized microwave annealing parameters are necessary to realize fabrication of devices with excellent device performance and reliability.

6. Correlation of Strain and Bias in AlGaN/GaN Heterostructured devices

Introduction

This Chapter deals with the characterization of Aluminum Gallium Nitride/Gallium Nitride (AlGaN/GaN) based devices. Recently, AlGaN/GaN high electron mobility transistors (HEMT) have become important because of their potential applications in electronic, optoelectronic, high-temperature, and high-power devices [44,45]. AlGaN/GaN HEMTs have the desirable characteristics to replace GaAs based power amplifiers due to the very high breakdown field of GaN which is estimated to be 3MV/cm [46]. However, heteroepitaxially grown GaN tends to have structural defects arising due to mismatch in lattice parameters and, difference in coefficients of thermal expansion between the GaN epilayers and the substrates such as silicon carbide or sapphire.

Significant progress has been made in the fabrication and electrical characterization of the HEMT devices [45,47- 50]. The AlGaN/GaN HEMT structures have shown high electron mobility (>1500 $cm^2/V.s$) resulting in low specific resistivity values. However, for achieving more reliable device yields it is important to have homogeneity in electrical transport properties across the entire wafer. To improve the

device performance and reliability, it is important to know the reasons for the variation in the electrical properties across the wafer. In this work, the spatial variation of in-plane strain in the GaN channel region of the HEMT devices is correlated with the variation in device channel resistance across the wafer. The localized lattice parameters and rocking curves at each point were measured to determine microscopic strain, crystalline quality and dislocation density. These point-wise strain measurements were used for comparison with the corresponding channel resistance measurements. Furthermore, these measurements are benign to the overall device performance and are non-destructive in nature. Hence, the x-ray micro-diffraction technique is unique in providing much needed information on the range of variation in electrical characteristics of the HEMT devices on the wafer even before the devices are made.

It has been known that both for zinc-blende semiconductors with a (111) orientation [51] as well as for III-nitrides with a (0001) orientation [52] that piezoelectric effects can vary the charge density and electric field distributions within these materials. It has been shown that piezoelectric polarization in hexagonal AlGaN/GaN heterostructures leads to an increase in the carrier concentration at the interface [53- 57]. In addition, pseudomorphically grown AlGaN/GaN layers have strain, which contributes to a piezoelectric field at the interface. It has also been reported that due to this polarization, the electron and hole wave functions are spatially separated in the AlGaN/GaN quantum well thereby affecting the 2d electron gas (2DEG) [58].

Furthermore the polarization effects due to piezoelectric fields and other surface states in AlGaN/GaN HEMT devices have been reported and correlated to the density of

the 2DEG [59,60]. They show a significant increase in the carrier concentration as a result of increase in the strain induced piezoelectric charge at the AlGaN/GaN interface. It has been found in these studies that both when the Al concentration is increased or when the AlGaN layer thickness is increased the piezoelectric charge increases due to the strain at the AlGaN/GaN interface. This was experimentally verified by measuring the 2DEG density as a function of the AlGaN layer thickness. The 2DEG density increases initially due to an increase in the carrier concentration but starts to decrease later due to an increase in carrier scattering effects.

Although the correlation of strain induced piezoelectric charges and carrier concentration at the AlGaN/GaN interface has been studied, it is important to know the variation in the strain with applied bias in these devices. This would provide further insight into the 2DEG density in the GaN channel and the transport properties of the AlGaN/GaN devices. In this work, the variation in strain due to the change in bias applied to the AlGaN/GaN Schottky diodes was studied. Using in-situ high resolution x-ray micro-diffraction technique, the localized strain, and the respective rocking curves of the GaN channel were obtained. This non-destructive technique is very useful because it provides the bias dependant variation in the material parameters, within the active device region. Additionally, the extrapolated piezoelectric charges from the strain measurements were correlated with the bias applied to the device.

6.1 Surface Strain and its Impact on the Electrical Resistivity in GaN channel of AlGaN/GaN HEMT

6.1.1 Experimental Procedure:

The AlGaN/GaN HEMT wafer was grown epitaxially on silicon carbide substrate. A 0.1μm AlN nucleation layer was deposited followed by an unintentionally doped 1μm GaN buffer/channel layer, and an undoped 250 Å $Al_{0.25}Ga_{0.75}N$ layer. The devices were fabricated using traditional photolithography and liftoff process. Ni/Au was used for the Schottky gate metal and Ti/Al/Ni/Au was used for the ohmic contacts.

High resolution x-ray diffraction (HRXRD) and rocking curve measurements were performed using the triple axis four-circle Rigaku ATX-E diffractometer. In order to get the localized lattice parameters, strain, and the rocking curves from a specific section of the wafer, incident beam slits were used to collimate the incident x-ray beam and diffraction spectrum was obtained only from the required area on the sample. These results from the specific regions of the wafer were then compared with the corresponding electrical measurements.

The sheet resistance map was obtained by device *I-V* measurements across the entire wafer.

6.1.2 Results and Discussion

Figure 27 shows a rocking curve measured for the (004) reflection of the GaN channel in the HEMT device wafer. The FWHM value is ~200 arcseconds, suggesting the dislocation density of ~$1x10^8$ lines/cm^2, which could be attributed to the strain arising due to lattice mismatch of GaN with the substrate [61-63]. The average crystallite size was calculated to be ~ 100 nm from the Scherrer equation.

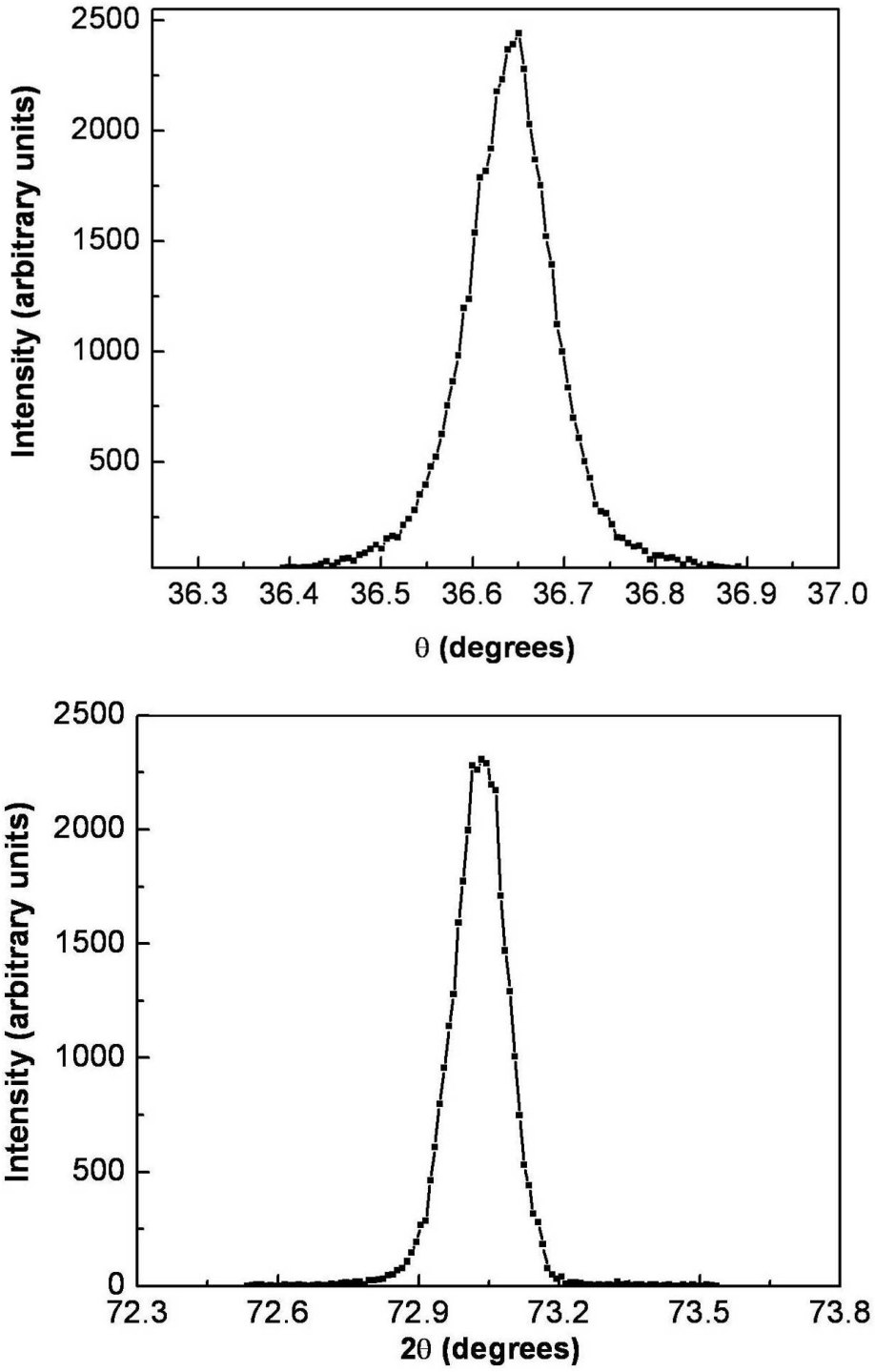

Figure 27: High resolution x-ray rocking curve (top) and high resolution x-ray diffraction spectra (bottom) of GaN from AlGaN/GaN HEMT wafer.

The high resolution x-ray micro-diffraction measurements taken as a function of the (x,y) coordinates on the (004) reflection of the GaN channel provide the spatial *c*-lattice parameters. The out of plane and the in-plane strain are computed using the relations:

$$\varepsilon_{\perp} = \frac{\Delta c}{c}, \tag{25}$$

and

$$\varepsilon_{\parallel} = -\nu\varepsilon_{\perp}, \tag{26}$$

where $\varepsilon_{\perp}$ is the out of plane strain, $\varepsilon_{\parallel}$ is the in-plane strain, and ($\nu = 0.183$) is the poisson's ratio of GaN [64]. The measured in-plane strain was in the range of $2.295\text{x}10^{-4}$ – $3.539\text{x}10^{-4}$ and the resistivity was in the range of 345 – 411 Ω/□. The spatially resolved in-plane strain is compared one-to-one with the resistivity measurements of the HEMT devices on the wafer. Figure 28 and figure 29 show the spatial map of the in-plane strain and the measured electrical resistivity, respectively. It can be seen from figures 28 and 29 that the variation in the in-plane strain correlates well with the variation in the electrical resistivity of the sample. This result shows that the effect of tensile strain in the GaN channel may result in a change of electrical resistivity.

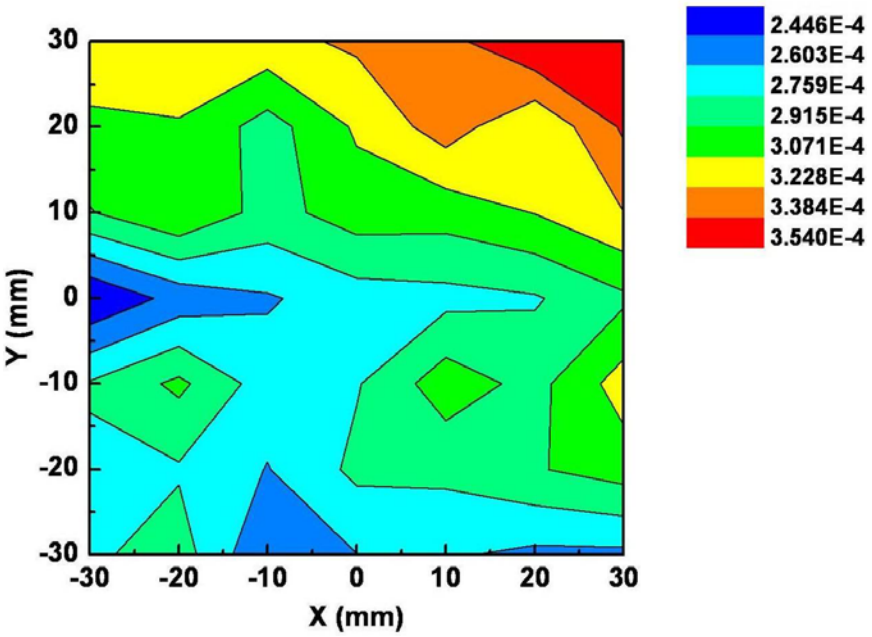

Figure 28: Spatial distribution of the in-plane strain in GaN as measured by x-ray diffraction on AlGaN/GaN HEMT wafer.

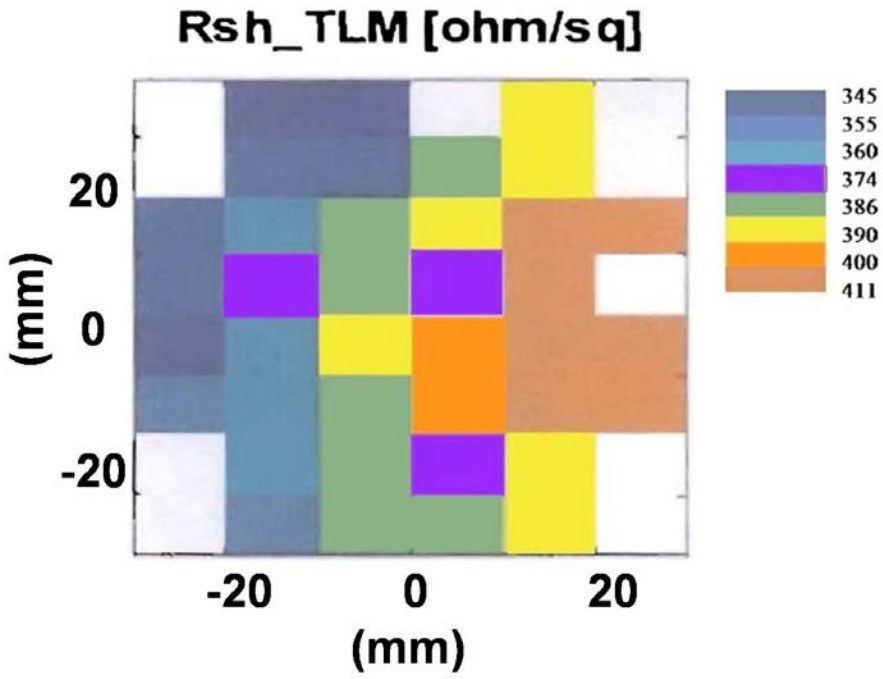

Figure 29: Spatial distribution of the sheet resistance on the AlGaN/GaN HEMT wafer.

It has been shown that the resistivity of semiconductor materials increases exponentially with the increase in tensile strain [65]. The strain may be due to a combination of different factors in the fabrication of the HEMT devices. The hetero-epitaxial growth of the GaN channel region on the substrate, surface polishing, and interfacial defects such as interface roughness between AlGaN and GaN may cause strain in the GaN channel. Schottky gate metallization on AlGaN also contributes to the strain. Non uniformities in AlGaN gate, the gate metal, GaN channel layer thickness can lead to variation in strain across the wafer. If these measurements are performed on the samples after growing each layer it is possible to find out cause for the major contribution of the strain variation across the wafer. The non-destructive x-ray micro-diffraction measurements of the lattice parameters provide a comprehensive analysis of the localized strain. These results suggest that in order to have homogenous transport properties across the wafer, the growth parameters of AlGaN layer, GaN channel, and the buffer layer have to be optimized to reduce the strain and the strain variation across the wafer. This study proves that x-ray micro-diffraction mapping is a useful tool in screening wafers for achieving uniformity in electrical characteristics across the wafer. These unique measurements can provide guidance in the fabrication of the AlGaN/GaN based devices and on the areas to be improved and optimized in order to increase the wafer yield and in improving the performance of the device.

6.2 In-situ Strain Measurements on GaN/AlGAN Hetrostructure Schottky Barrier Diodes under Variable Bias Conditions

6.2.1 Experimental Procedure

The AlGaN/GaN samples were grown epitaxially on sapphire substrate using metalorganic chemical vapor deposition (MOCVD) technique. An unintentionally doped 2μm thick GaN channel layer was grown followed by an undoped 250 Å $Al_{0.25}Ga_{0.75}N$ layer. The Schottky diodes were fabricated by lift-off lithography using Ni/Au metallization. The diode structure consists of 115 μm diameter Schottky dots separated from the field metal by exposed (lifted-off metal) ring areas. The separation between a dot and the field metal area is 70 μm. The field metal surrounding the exposed ring regions is considered as the body metal contact for the semiconductor. This structure inherently has a high series resistance due to the field metal being on the AlGaN layer, which results in a large forward voltage drop. The series resistance was measured from the inverse slope of the linear segment of the forward *I-V* characteristics, shown in figure 30, and was found it to be ~ 2.7 kΩ.

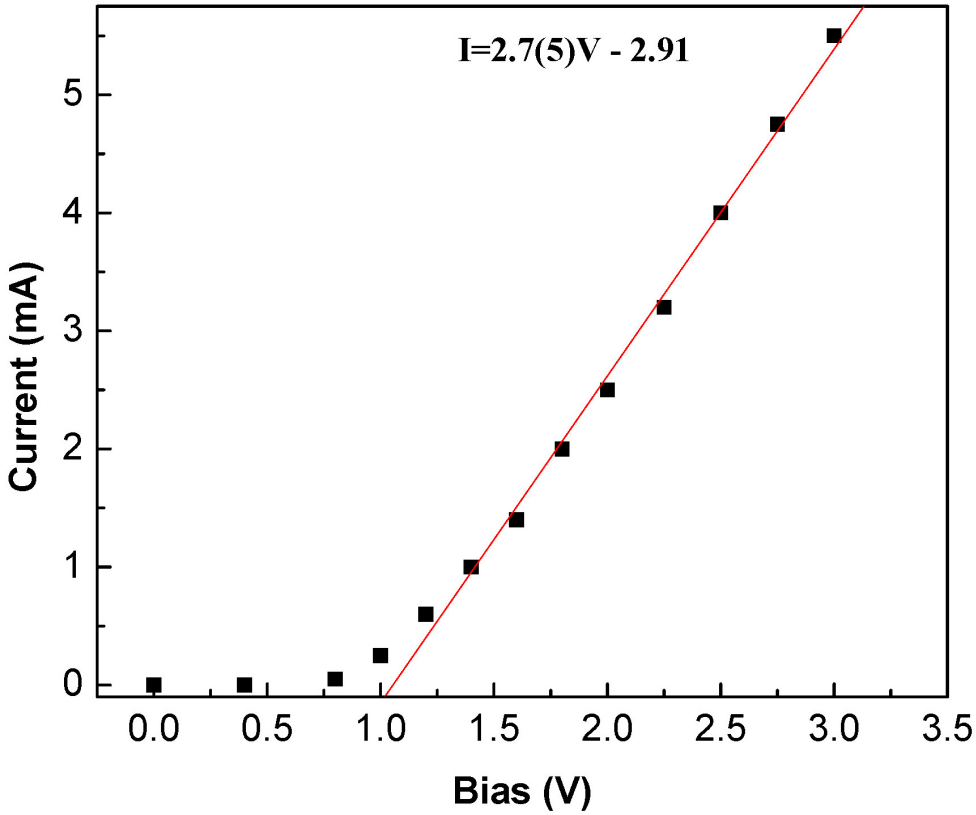

Figure 30: Forward I-V curve of the AlGaN/GaN Schottky diode

High-resolution x-ray rocking curve measurements were made using the triple axis four-circle Rigaku ATX-E diffractometer. In order to obtain the rocking curves from the region of the device under bias, the incident beam slits were used to collimate the incident x-ray beam to get diffraction only from the area of interest on the sample. X-ray rocking curves were measured by varying bias conditions. Thus, the measured rocking curves provide structural information on strain located in the device area under variable bias conditions.

A Tektronix Type 576 Curve tracer was used to apply/measure the bias applied in-situ during the high resolution x-ray measurements. Wire bonding was performed in order to make contacts to the Schottky diode dots and the GaN body contact. Forward bias was applied in the range of 0 to 10 V and reverse bias was applied in the range of 0 to -100 V. Large forward bias is the result of large series resistance between the electrodes of the diode. The device under bias was allowed to settle for 10 s before making the x-ray measurements.

6.2.3 Results and Discussion

Figure 31 shows a rocking curve measured for the (004) reflection of the GaN channel under no bias condition. The FWHM value is ~300 arcseconds suggesting a dislocation density of ~$2x10^8$ lines/cm^2 and this high dislocation density is attributed to the strain arising due to lattice mismatch of GaN with the sapphire substrate and the AlGaN/GaN interface [61]. The average crystallite size was calculated to be ~ 100 nm from the Scherrer equation.

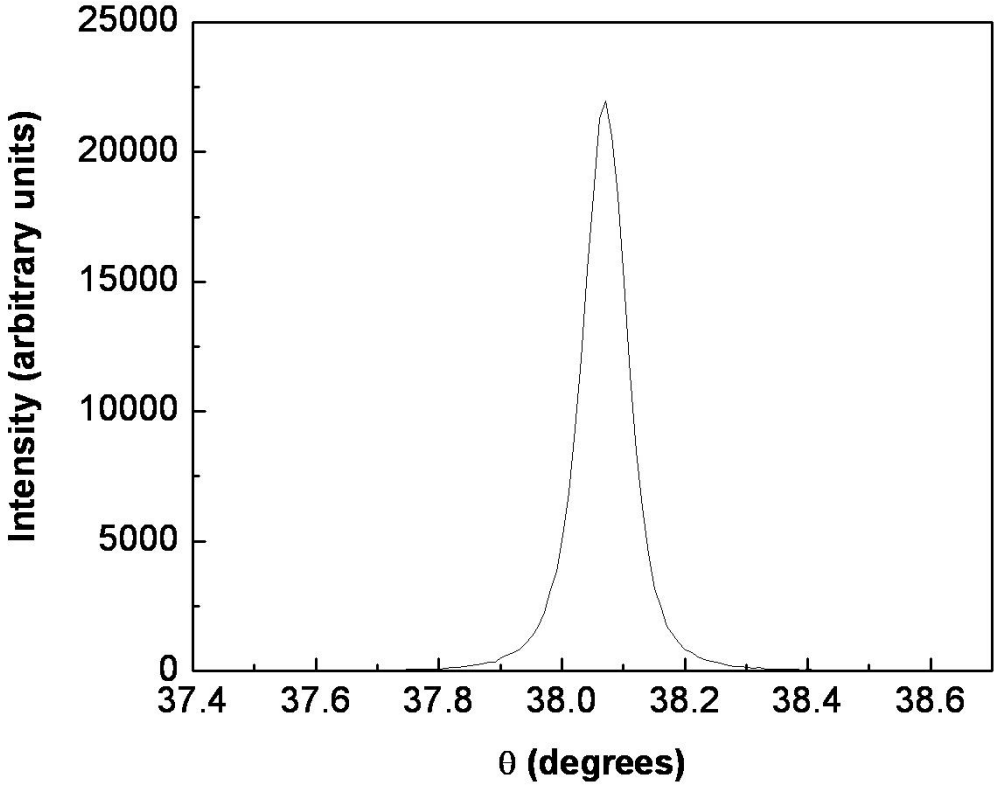

Fig. 31: High resolution x-ray rocking curve of GaN from AlGaN/GaN devices.

The Schottky diodes were forward biased in the range of 0 to 10V and reverse biased in the range of 0 to -100V, and the corresponding *in-situ* x-ray rocking curves were recorded as a function of variable bias. Figure 32 shows the rocking curves obtained for various bias conditions of the GaN channel region. It can be seen from figure 32a that on application of forward bias the peak position shifts towards the high-angle side indicating an increase in the compressive strain in the perpendicular direction of the GaN channel region, whereas application of reverse bias, as seen in figure 32b, causes an opposite shift in the rocking curves, which reflects a tensile strain in the GaN channel.

The compressive to tensile shift in strain with bias polarity change is due to piezoelectric behavior of AlGaN/GaN heterojunction.

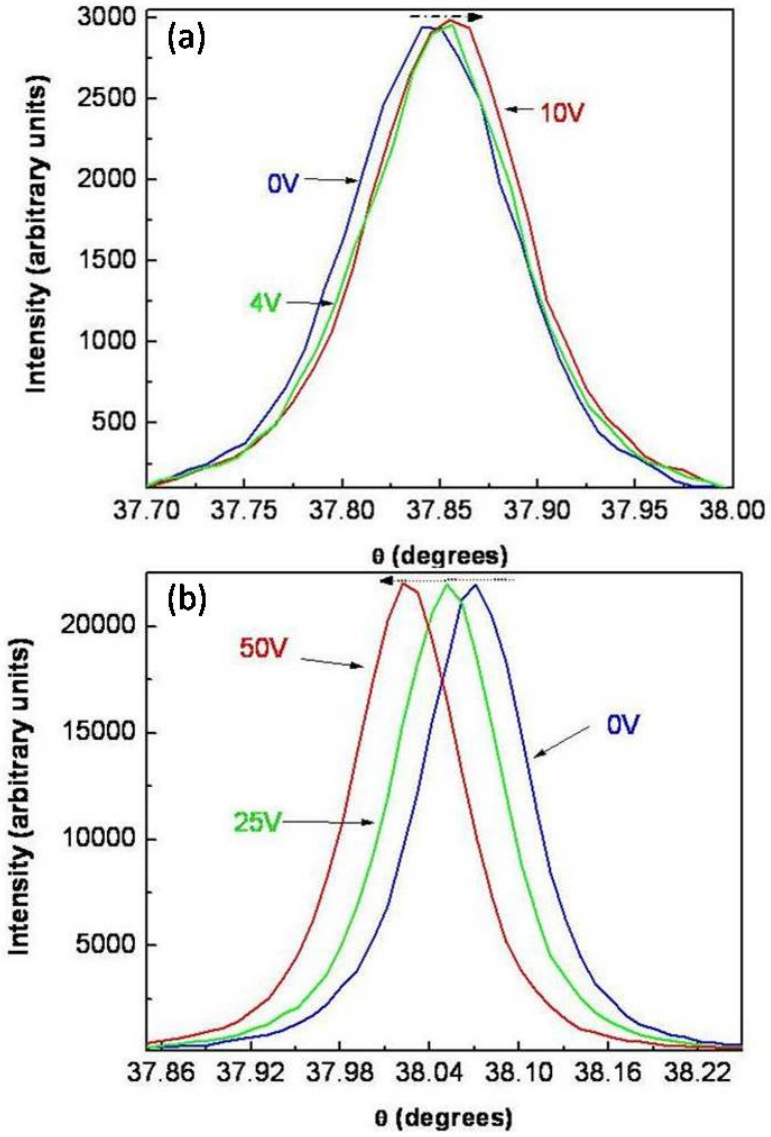

Fig. 32: Change in the rocking curves positions with applied (a) forward and (b) reverse bias for the GaN channel of the AlGaN/GaN Schottky diodes.

The out of plane strain, $\varepsilon_\perp$ is computed using equation (27) and the in-plane strain $\varepsilon_\parallel$ is related to $\varepsilon_\perp$ by equation (28) [66]

$$\varepsilon_\perp = -\frac{\Delta\theta}{\tan\theta}, \tag{27}$$

and $$\varepsilon_\parallel = -\nu\varepsilon_\perp, \tag{28}$$

where θ is the Bragg angle, and ν (= 0.183) is the poisson's ratio for GaN. For the forward bias measurements in the range of 0 to 10 V the in-plane strain variation was in the range of $1.7\text{x}10^{-5}$ – $3.36\text{x}10^{-5}$, and for the reverse bias of 0 to -100V the strain variation was in the range of $-7.7\text{x}10^{-5}$ to $-111.4\text{x}10^{-5}$. Figure 33 shows the variation of the in-plane strain with forward and reverse bias. It can be seen from figure 33(a) that the strain is positive, which reflects increasing tensile strain in the GaN channel, whereas in figure 33(b) the strain is negative and decreasing, which means that a compressive strain is developed in the GaN channel. Also in figure 33(b) a discontinuity is observed in the strain after -50V, which is due to the depletion of the entire GaN layer causing considerably high strain in the material. The depletion width with applied bias for a Schottky diode is calculated using the relation:

$$W = \left[\frac{2\varepsilon(V_o - V)}{q}\frac{1}{N_d}\right]^{1/2}, \tag{29}$$

where ε (= $8.41\text{x}10^{-13}$ F/cm) is the permittivity of GaN, q is the electric charge, and N_d ($\sim 10^{16}$ /cm^3) is the doping concentration. The depletion width for 50 V reverse bias is calculated to be 2.2 μm, which is roughly the thickness of the GaN layer for this device structure.

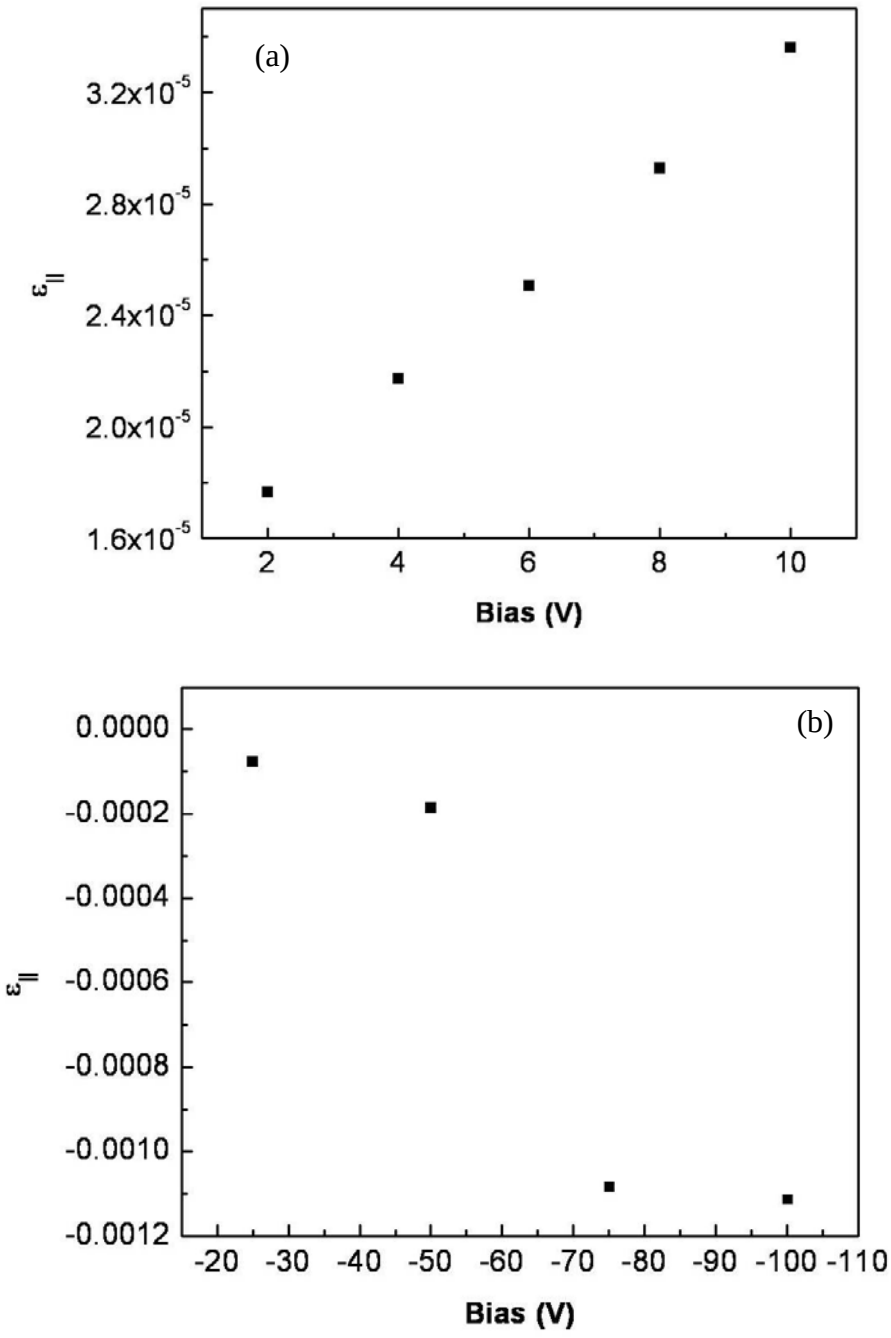

Fig. 33: The in-plane strain in the GaN channel with applied (a) forward bias, and (b) reverse bias.

Using least square fitting the following equations were obtained for the in-plane strain:

For forward bias: $\varepsilon_{\parallel} = 1.3652x10^{-5} + 1.9715x10^{-6}V$ (30)

For reverse bias < 50V: $\varepsilon_{\parallel} = 3.1899x10^{-5} - 4.3545x10^{-6}V$ (31)

The piezoelectric polarization in a strained material can be computed using the relation [60]:

$$P_{PE} = e_{33}\varepsilon_{\perp} + 2e_{31}\varepsilon_{\parallel} \quad (32)$$

where e_{33} (=1 C/m^2) [67] and e_{31} (= -0.49 C/m^2) [68] are piezoelectric coefficients of GaN. The AlGaN/GaN interface has much higher piezoelectric polarization compared to other III-nitride semiconductor heterostructures even at zero bias due to strain at the interface. In this study the strain relative to the strain at zero bias is measured for the calculation of the piezoelectric polarization. Also, assuming that all the bias induced strain may contribute to the piezoelectricity, the upper limit of the polarization field is found to be in the range of -1.1x10^{-4} to -2.1x10^{-4} C/m^2 for forward bias and 5x10^{-4} C/m^2 to 12x10^{-4} C/m^2 for reverse bias before the possible depletion of the entire GaN layer. The maximum change in the sheet carrier concentration is calculated using the relation:

$$\Delta n_s = \frac{P_{PE}}{e} \quad (33)$$

The change in the sheet carrier concentration with applied bias is found to be in the range of 10^{10} to 10^{12} cm^{-2}. This change in the sheet concentration is significant for reliable

of the strain in an operating AlGaN/GaN HEMT device on the effective 2DEG density needs to be considered for an accurate device modeling.

Summary of the results

The high-resolution x-ray diffraction and rocking curve measurements were performed on AlGaN/GaN HEMT devices as a function of (x, y) coordinates on the wafer. Based on these measurements, the average dislocation density is estimated to be of the order of 10^8 lines/cm^2. The localized in-plane strain was found to be tensile in nature for the GaN channel region of the AlGaN/GaN HEMT devices and in the range of $2.295 \times 10^{-4} - 3.539 \times 10^{-4}$. The corresponding electrical resistivities were in the range of 345 – 411 Ω/□. The spatial map of the in-plane strain and the electrical resistivity map of the wafer showed one-to-one correspondence. The origin of the in-plane tensile strain can be attributed to a combination of different factors such as random array of dislocations, surface polishing, lattice and thermal mismatch in the GaN channel/buffer region of the HEMT device.

The high-resolution x-ray rocking curve measurements were performed *in situ* on AlGaN/GaN Schottky diodes as a function of applied bias for the first time. The in-plane strain for the GaN channel region of the AlGaN/GaN Schottky diodes as a function of the applied forward and reverse bias was in the range of $1.7 \times 10^{-5} - 3.36 \times 10^{-5}$ for 0 to 10 V forward bias and -7.7×10^{-5} to -111.4×10^{-5} for the reverse bias of 0 to -100V. The strain was found to vary linearly with increasing bias, but there was a discontinuity in the strain measurements for reverse bias greater than 50V due to possible depletion of the entire

GaN layer. The upper limit for piezoelectric polarization due to the bias induced strain is calculated and found to be in the range of -1.1×10^{-4} to -2.1×10^{-4} C/m^2 for forward bias and 5×10^{-4} C/m^2 to 12×10^{-4} C/m^2 for reverse bias before the entire GaN layer is depleted. This polarization causes a change in the sheet carrier concentration in the range of 10^{10} to 10^{12} cm^{-2}, which may cause a variation in the 2DEG density in the GaN channel of the AlGaN/GaN devices. The variation in the 2DEG density due to the bias induced strain may result in unpredictable operation of the device and needs to be considered for the correct modeling of the device transport characteristics.

7. CONCLUSIONS AND FUTURE WORK

7.1 Conclusions

In this work, the defects in wide bandgap semiconductor materials were studied using non destructive characterization techniques. Novel x-ray characterization methods were used for the first time in order to study the uniformity of strain in AlGaN/GaN device structures across the wafer and the results were correlated with device electrical characteristics. Additionally, bias induced strain in AlGaN/GaN Schottky diodes was measured, and the results were correlated with the change in the piezoelectric charges at the AlGaN/GaN interface. This phenomenon was studied for the first time, in this work. Results of this work can be used in order to optimize the modeling and growth/processing conditions of AlGaN/GaN devices.

Defects in freestanding GaN films were studied using high resolution x-ray diffraction, grazing angle diffraction and x-ray topography. Anisotropic depth dependant in-plane strain measured in these films was found to be 4.0791×10^{-3} up to a depth of 0.3 μm. High resolution x-ray topography studies provided a comprehensive map of defects on the GaN films. The HRXT images showed presence of ridges, and cavities in these films. Warpage was found in these films in the order of 0.5 m, which is detrimental to the yield of devices fabricated on these films.

Virgin and Al ion-implanted 4H-SiC epitaxially grown films were characterized using x-ray diffraction and rocking curve measurements to optimize the microwave annealing parameters for best crystalline quality of the SiC films. Post implant microwave annealed samples in the temperature range of 1700 ^{o}C – 1900 ^{o}C for 30 s duration were used in this work. The x-ray diffraction measurement spectra show that the microwave annealing process is successful in removing the lattice damage and in activating the implant. From the FWHM values of the microwave annealed samples, it can be seen that there is a significant improvement in the crystalline quality of the SiC samples. The sample annealed at 1900 ^{o}C had the best rocking curve FWHM of 9 ± 2 arcsecs, which not only confirmed annihilation of the defects introduced during the Al^{+} ion-implantation process, but also an improvement in crystalline quality over the as-grown virgin 4H-SiC sample that had a rocking curve FWHM of 18.7 ± 2 arcsecs.

Single-energy Mg ion-implantation doped GaN films, characterized by using x-ray diffraction measurements after microwave annealing in the temperature range of 1300 ^{o}C – 1500 ^{o}C for 15 s, showed activation of the Mg implant through the disappearance of the sub-lattice peak observed in the as-implanted sample. From the rocking cuve FWHM values, the 15 s annealing showed an improvement in the crystalline quality of the GaN samples as compared to the as-implanted samples. Also electrical conductivity was observed in these samples due to Mg implant activation.

The x-ray measurements performed on the AlGaN/GaN device structures show the effect of localized strain on the sheet resistance across the wafer. The map of in-plane strain in the AlGaN/GaN HEMT wafer was measured for the first time and it showed a

near one-to-one correspondence with the variation in device channel sheet resistance. The in-plane strain variation is in the range of 2.295×10^{-4} – 3.539×10^{-4} resulting in a sheet resistance variation of 345 - 411 Ω/□.

The in-situ high resolution x-ray diffraction measurements, performed on the AlGaN/GaN Schottky diodes under variable bias conditions, showed in-plane tensile strain for forward bias conditions, and compressive strain for reverse bias. A linear variation in the strain was observed with the bias voltage, which resulted in a change in the piezoelectric charge in the range of -1.1×10^{-4} to -2.1×10^{-4} C/m^2 for forward bias and 5×10^{-4} C/m^2 to 12×10^{-4} C/m^2 for reverse bias. The change in the sheet carrier concentration with the applied bias was found to be in the range of 10^{10} to 10^{12} cm^{-2}. This variation needs to be considered for the correct modeling of the device transport characteristics.

7.2 Future Work

It has been shown by in-situ x-ray diffraction, that the application of bias causes a change in the piezoelectric charge at the AlGaN/GaN interface. This effect has to be accounted for in the device models. Modeling parameters have to be developed in order to account for the change in sheet carrier concentration of these devices with gate bias voltage. Also, the relation of this effect to the current and power densities need to be studied. The first step in order to perform this modeling, is to make similar measurements on several high quality AlGaN/GaN device structures grown using different techniques. The results have to be analyzed carefully and correlated with the applied bias. After

obtaining more results, the individual contributions of the interface strain such as the piezoelectric effects, spontaneous polarization effects, etc. need to be identified. These effects can then be added to the device models. Additional measurements such as in-situ x-ray topography with variable bias at a synchrotron source should also be performed to confirm these results.

The piezoelectric effect at the AlGaN/GaN interface is very high and can be used for some novel applications. The effect of high pressure in this material is not studied and may result in some unique findings. If sufficient strain is developed as a result of application of high pressures, this might lead to creation of a piezoelectric charge at the AlGaN/GaN interface and this charge in turn may yield current flow. High pressure x-ray diffraction studies of this material in a diamond anvil cell should be carried out to find this potential application.

With respect to acceptor implantation doping in GaN films, a detailed study involving different doping concentrations need to be studied for developing ion implantation conditions for efficient p-type doping.

LIST OF REFERENCES

LIST OF REFERENCES

[1] S. Nakamura, G. Fasol, The blue laser diode – GaN based light emitters and lasers, Springer, Berlin, (1997)

[2] M. A. Kahn, M. S. Shur, J. N. Kuznia, Q. Chen, J. Burm, W. Schaff, Appl. Phys. Lett. **63** (1993) 1214

[3] S.J. Pearton, C.R. Abernathy, F. Ren, Gallium Nitride Processing for Electronics, *Sensors, and Spintronics*, Springer-Verlag, London (2006)

[4] Z. C. Feng (ed.), *III-Nitride Semiconductor Materials*, Imperial College Press. London (2006)

[5] C.E. Weitzel, J.W. Palmour, A.H. Carter, K. Moore, K.K. Nordquist, S. Allen, C. Thero, M. Bhatnagar, IEEE Trans. Electron Dev. **43** (1996) 1732

[6] T.D. Moustakas, T. Lei, R.J. Molnar, Physica B **185** (1993) 36

[7] Hermann M, Gogova D, Siche D, Schmidbauer M, Monemar B, Stutzmann M, Eickhoff M, J. Crystal Growth **293** (2006) 462-468

[8] X.A. Cao, J.M. Teetsov, M.P. D'Evelyn, D.W. Merfeld, C.H. Yan, Appl. Phys. Lett. 85 (2004) 7

[9] G. Franssen, S. Grzanka, R. Czernecki, T. Suski, L. Marona, T. Riemann, J. Christen, H. Teisseyre, P. Valvin, P. Lefebvre, P. Perlin, M. Leszczynski, I. Grzegory, J. Appl. Phys. 97 (2005) 103507

[10] M. Misheva, H. Larsson, D. Gogova, B. Monemar, Phys. Stat. Sol. (a) 202 (2005) 713

[11] S.C Singhal, *J. Mater. Sci.* **11** (1976) 1246

[12] G. Pensl, V. Afanasev, M. Bassler, M. Schadt, T. Troffer, J. Heindl, H. Strunk, M. Maier, and W. Choyke, *Inst. Phys. Conf. Ser.* **142** (1996) 275

[13] J.B. Tucker, S. Mitra, N. Papanicolaou, A. Siripuram, M.V. Rao, O.W. Holland, Diamond Relat. Mater **11** (2002) 392

[14] S-H. Ryu, S. Krishnaswami, M. O'Loughlin, J. Richmond, A. Agarwal, J. Palmour, A.R. Hefner, IEEE Electron Device Lett. **25** (2004) 556

[15] M. J. Hordon, and B. L. Averbach, Acta Metall. **9** (1961) 237

[16] W.L. Bragg, Proceedings of the Cambridge Philosophical Society, **17** (1913), 43

[17] R. Lang, J. Appl. Phys. **30** (1959) 1748

[18] G.H. Schwuttke, Gen. Tel. Elec. Develop. J. **1** (1961) 68

[19] J. B. Newkirk, Trans. AIME **215** (1959) 483

[20] J.P. Yesinowski, phys. stat. sol. (c) **2** (2005) 2399

[21] Yesinowski, J.P.; Purdy, A.P.; Wu, H.; Spencer, M.G.; Hunting, J.; DiSalvo, F.J, J. Am. Chem. Soc. March 2006

[22] T. Hashimoto, K. Fujito, F. Wu, B. A. Haskell, P. T. Fini, J. S. Speck and S. Nakamura, Jpn. J. Appl. Phys. **44** (2005) L797

[23] Z. Liliental-Weber, Y. Chen, S. Ruvimov, and J. Washburn, Phys. Rev. Lett. **79** (1997) 2835

[24] F. A. Ponce, D. Cherns, W. T. Young, and J. W. Steeds, Appl. Phys. Lett. **69** (1996) 770

[25] H. Juza, Z. Anorg. Chem. **239** (1938) 285

[26] Slichter, C.P. *Principles of Magnetic Resonance,* 3d ed., Springer Series in Solid-State Sciences, Springer-Verlag NY (1989)

[27] Yesinowski, J.P., J. Magn. Reson., **180** (2006) 147

[28] G. H. Schwuttke, J. Appl. Phys. **36** (1965) 2712

[29] P. Gay, P. B. Hirsch, and A. Kelly, Acta Metall. **1** (1953) 315

[30] M. J. Hordon, and B. L. Averbach, Acta Metall. **9** (1961) 247

[31] S. B. Qadri, and J. H. Dinan, Appl. Phys. Lett. **47** (1985) 1066

[32] J. Elsner, R. Jones, P. K. Sitch, V. D. Porezag, M. Elstner, and Th. Frauenheim, M. I. Heggie, S. Öberg, and P. R. Briddon, Phys. Rev. Lett. **79** (1997) 3672

[33] P. Scherrer, Nachr. Gottingen, **2** (1918) 98

[34] T. Matsubara and K. Shoda, Jpn. J. Appl. Phys. **45** (2006) 279

[35] J. Senzaki, K. Fukuda, K. Arai, J. Appl. Phys. **94** (2003) 2942

[36] S. G. Sundaresan, M. V. Rao, Y. L. Tian, J. A. Schreifels, M. C. Wood, K. A. Jones, A. V. Davydov, J. Elec. Mater. **36** (2007) 324

[37] S. G. Sundaresan, Y. L. Tian, J. A. Schreifiels, J. J. Kopanski, M. V. Rao, J. Appl. Phys. **101** (2007) 073708

[38] B. E. Warren, X-ray Diffraction, Chap. 14 (1990)

[39] S. G. Sundaresan, Y. L. Tian, M. C. Ridgeway, N. A. Mahadik, S. B. Qadri, M. V. Rao, Nuc. Inst. Meth. B **261** (2007) 616

[40] B. D. Culity, Elements of X-ray Diffraction (2001)

[41] C. Ronning et al. Phys. Reports **351** (2001) 349

[42] R.Y. Korotkov, J.M. Greigie, B.W. Wessels, *Appl. Phys. Lett.* **78** (2001) 222

[43] H.Y.A. Chung et al. *J. Crys. Growth* **230** (2001) 549

[44] U. K. Mishra, P. Parikh, and Y. F. Wu, Proceedings of the IEEE, **90** (2002) 1022

[45] G.H. Jessen, R.C. Fitch, J.K. Gillespie, G.D. Via, N.A. Moser, M.J. Yannuzzi, A. Crespo, J.S. Sewell, R.W. Dettmer, T.J. Jenkins, R.F. Davis, J. Yang, M.A. Khan, S.C. Binari, IEEE Elec. Dev. Lett. **24** (2003) 677

[46] V. A. Dmitriev, K.G. Irvine, C.H. Carter, N.I. Kuznetsov, E.V. Kalinina Appl. Phys. Lett. **68** (1996) 229

[47] S.C. Binari K. Ikossi, J.A. Roussos, W. Kruppa, D. Park, H.B. Dietrich, D.D. Koleske, A.E. Wickenden, R.L. Henry, IEEE Trans. Elec. Dev. **48** (2001) 465

[48] D.S. Katzer, S.C. Binari, D.F. Storm, J.A. Roussos, B.V. Shanabrook, E.R. Glaser, Elec. Lett. **38**, 1740 (2002)

[49] P.B. Klein, J.A. Mittereder, S.C. Binari, J.A. Roussos, D.S. Katzer, D.F. Strom, Elec. Lett. **39** (2003) 1354

[50] A.P. Edwards, J.A. Mitereder, S.C. Binari, D.S. Katzer, D.F Storm, J.A. Roussos, IEEE Elec. Dev. Lett. **26** (2005) 225

[51] E. A. Cardi, T. Y. Chang, K. W. Goosen, and L. F. Eastman, Appl. Phys. Lett. **56** (1990) 659

[52] W. Q. Chen, and S. K. Hark, J. Appl. Phys. **77** (1995) 5747

[53] Bykhovski, B. L. Gelmont, and M. S. Shur, J. Appl. Phys. **81** (1997) 6332

[54] P. M. Asbeck, E. T. Yu, S. S. Lau, G. J. Sullivan, J. Van Hove, and J. M. Redwing, Elect. Lett., **33** (1997) 1230

[55] E. T. Yu, G. J. Sullivan, P. M. Asbeck, C. D. Wang, D. Qiao, and S. S. Lau, Appl. Phys. Lett., **71** (1997) 2794

[56] M. B. Nardelli, K. Rapcewicz, and J. Bernholc, Appl. Phys. Lett **71** (1997) 3135

[57] T. Takeuchi, H. Takeuchi, S. Sota, H. Sakai, H. Amano, and I. Akasaki, Jpn. J. Appl. Phys. Part 2, **36** (1997) L177

[58] Hangleiter, J. S. Im, H. Kollmer, S. Heppel, J. Off, and F. Scholz, MRS Internet J. Nitride Sem. Res. **3** (1998) 15

[59] J. P. Ibbetson, P. T. Fini, K. D. Ness, S. P. DenBaars, J. S. Speck, and U. K. Mishra, Appl. Phys. Lett. **77** (2000) 250

[60] O. Ambacher, J. Smart, J. R. Shealy, N. G. Weimann, K. Chu, M. Murphy, W. J. Schaff, L. F. Eastman, R. Dimitrov, L. Wittmer, Stutzmann, W. Rieger, and J. Hilsenbeck, J. Appl. Phys. **85** (1999) 3222

[61] P. Gay, P. B. Hirsch, and A. Kelly, Acta Cryst. **7** (1954) 41

[62] M. J. Hordon, and B. L. Averbach, Acta Metall. **6** (1958) 446

[63] S. B. Qadri, and J. H. Dinan, Appl. Phys. Lett. **47** (1985) 1066

[64] M.A. Moram, Z.H. Barber, C.J. Humphreys, J. Appl. Phys. **102** (2007) 23505

[65] R. Gosh, D. Basak, S. Fujihara, J. Appl. Phys. **96** (2004) 2689

[66] D. I. Ma, S. B. Qadri, M. C. Peckerar, and D. McCarthy, Thin Sol. Films, **206** (1991) 18

[67] G. D. O'Clock, and M. T. Duffy, Appl. Phys. Lett. **23** (1973) 55

[68] F. Bernardini, V. Fiorentini, and D. Vanderbilt, Phys. Rev. B **56** (1997) 10024

CURRICULUM VITAE

Nadeemullah Mahadik graduated with his Bachelors in electrical engineering from Old Dominion University, Norfolk, Virginia in 2003. He worked at George Mason University, Fairfax, Virginia as a graduate research assistant and conducted his research at the US Naval Research Laboratory, Washington, DC and at the National Institute of Standards and Technology, Gaithersburg, MD.